Filopodyan: An open-source pipeline for the analysis of filopodia

Vasja Urbančič,[1,2] Richard Butler,[1] Benjamin Richier,[1,2] Manuel Peter,[1,2] Julia Mason,[1,2] Frederick J. Livesey,[1,2] Christine E. Holt,[3] and Jennifer L. Gallop[1,2]

[1]Wellcome Trust/Cancer Research UK Gurdon Institute, [2]Department of Biochemistry, and [3]Department of Physiology, Development, and Neuroscience, University of Cambridge, Cambridge, England, UK

Filopodia have important sensory and mechanical roles in motile cells. The recruitment of actin regulators, such as ENA/VASP proteins, to sites of protrusion underlies diverse molecular mechanisms of filopodia formation and extension. We developed Filopodyan (filopodia dynamics analysis) in Fiji and R to measure fluorescence in filopodia and at their tips and bases concurrently with their morphological and dynamic properties. Filopodyan supports high-throughput phenotype characterization as well as detailed interactive editing of filopodia reconstructions through an intuitive graphical user interface. Our highly customizable pipeline is widely applicable, capable of detecting filopodia in four different cell types in vitro and in vivo. We use Filopodyan to quantify the recruitment of ENA and VASP preceding filopodia formation in neuronal growth cones, and uncover a molecular heterogeneity whereby different filopodia display markedly different responses to changes in the accumulation of ENA and VASP fluorescence in their tips over time.

Introduction

Cells form an extensive network of actin-rich protrusions to move through tissues, including veil-like lamellipodia and finger-like filopodia (Mattila and Lappalainen, 2008; Bisi et al., 2013; Krause and Gautreau, 2014; Jacquemet et al., 2015). Filopodia play key roles throughout embryonic development, including in the developing nervous system. Filopodia mediate the sensing of attractant and repellent guidance cues by growth cones (Zheng et al., 1996; McConnell et al., 2016) and the guidance of axons through the developing nervous system (Bentley and Toroian-Raymond, 1986; O'Connor et al., 1990; Chien et al., 1993). Once neurites arrive at their destination, filopodia are involved in the formation of branches (Dwivedy et al., 2007) and synaptic connections (Ziv and Smith, 1996; Lohmann and Bonhoeffer, 2008).

Despite the overwhelming importance of filopodia, many questions about their biology remain unanswered. First, the molecular mechanism of their formation is not clear. Multiple models have been proposed and experimentally supported, including (1) elongation of converging filaments within an underlying branched network of lamellipodial actin, fundamentally dependent on the Arp2/3 complex (Svitkina et al., 2003); (2) de novo nucleation of filopodial filaments at their tip by proteins also capable of promoting actin polymerization, such as formins (Faix and Rottner, 2006); and (3) initial clustering of membrane-binding proteins that subsequently recruit other factors required for filopodium formation (Lee et al., 2010; Saarikangas et al., 2015). However, the molecular identities of protein assemblies driving filopodium formation according to these models are not clear-cut. ENA/VASP proteins localize to filopodia tips upon their protrusion and are implicated in regulating the number and length of filopodia in a variety of cell types, through diverse mechanisms that structurally fit the "convergent elongation" and "tip nucleation" models (Lanier et al., 1999; Svitkina et al., 2003; Barzik et al., 2014). In retinal ganglion cells (RGCs), which we use here, ENA/VASP proteins are important for growth and stabilization of filopodia and terminal arborization of the axon (Dwivedy et al., 2007).

Moreover, it also appears that cells use multiple filopodial actin filament elongating proteins. Studies in *Drosophila melanogaster* and fibroblasts suggest that filopodia driven by ENA/VASP proteins or by formins (Dia/mDia2) have distinct properties (Barzik et al., 2014; Bilancia et al., 2014; Nowotarski et al., 2014). To better understand which proteins actively contribute to filopodia growth in various contexts, and to differentiate between models of filopodia formation, it would be critical to quantify the amount of proteins of interest within filopodia concurrently with their dynamic behavior. This approach has been very fruitful in understanding the protrusion of lamellipodia and membrane blebs (Charras et al., 2006; Machacek et al., 2009; Barry et al., 2015; Lee et al., 2015; Martin et al., 2016). A comprehensive image analysis pipeline is essential for these goals.

Recently, computational tools have been developed for automated segmentation and analysis of filopodia. These include MATLAB applications FiloDetect, which measures the

Correspondence to Jennifer Gallop: j.gallop@gurdon.cam.ac.uk

Abbreviations used: CCF, cross-correlation function; DCTM, direction-corrected tip movement; ED, erosion and dilation; HILO, highly inclined laminated optical sheet; iPSC, induced pluripotent stem cell; LoG, Laplacian of Gaussian; RGC, retinal ganglion cell; ROI, region of interest.

Supplemental material can be found at:
http://doi.org/10.1083/jcb.201705113

The Rockefeller University Press
J. Cell Biol.
https://doi.org/10.1083/jcb.201705113

number and lengths of filopodia in nonneuronal cells (Nilufar et al., 2013), and CellGeo, which allows identification and tracking of filopodia and the assessment of phenotypes in their morphodynamic properties, as well as characterizing lamellipodial dynamics (Tsygankov et al., 2014). The ImageJ plugin ADAPT identifies filopodia, among its suite of other functions, for automated quantification of cell migration and the dynamic behavior of lamellipodia and blebs in relation to their fluorescence intensities (Barry et al., 2015). Software has also been specifically designed for the automated detection of filopodia in dendrites, with a focus on their longitudinal and lateral movement (Hendricusdottir and Bergmann, 2014; Tárnok et al., 2015). Saha et al. (2016) pioneered concurrent analysis of fluorescence and filopodium behavior, developing MATLAB software for semiautomated analysis of filopodia dynamics and fluorescence. Most recently, the ImageJ plugin FiloQuant has enabled customizable automated quantification of filopodia lengths and densities, particularly in 3D microenvironments (Jacquemet et al., 2017 *Preprint*). Altogether, these studies demonstrate the surging demand for automated quantitative approaches in the field.

We built on these approaches by creating an ImageJ plugin for characterization of filopodia dynamics in parallel with the quantification of fluorescence, enabling us to determine the relationship between protein localization and filopodium behavior. Our plugin, Filopodyan, analyses fluorescence microscopy time-lapse datasets using the open-source platforms Fiji (Schindelin et al., 2012) and R (R Core Team, 2016). We have used Filopodyan to track the recruitment of ENA and VASP to newly forming filopodia and to filopodia tips during their extension and retraction. By quantifying the cross-correlation between fluorescence intensity and tip movement, we find several subpopulations of filopodia with different molecular behavior but similar morphological behavior.

Results

A customizable pipeline for automated identification of filopodia in time-lapse datasets

To allow the segmentation of filopodia within an image from the rest of the cell, we express a membrane marker within the cells of interest (Fig. 1 A). A membrane marker is more suitable for this purpose than a volume marker because of the high proportion of membrane to volume within filopodia relative to the rest of the cell, and we found that the uniform signal provided by a membrane marker performed better for reconstructions than an actin label (e.g., SiR-actin). The contrast between signal and background at the edges of the cell is further amplified by applying a Laplacian-of-Gaussian (LoG) filter to the image. This enhances the outline of the cell boundary and a thresholding method is then applied to create a mask of total cell area. The scale of the LoG filter (σ) and the choice of thresholding method are set by the user (initial guidelines for choice of parameters depending on pixel dimensions are provided in the User Guide). A graphical user interface window enables a rapid preview of segmentation, assisting the user to identify most suitable segmentation parameters before processing the entire image stack. Examples of different parameters and the suitability of a range of values are shown in Fig. 1 B. We also included adaptive thresholding as an option that may be useful for reconstructing low signal-to-noise images. Filopodyan was developed using images taken with a 100× objective using a CMOS camera with 65 nm pixel width. It is possible to segment filopodia at bigger pixel dimensions and consequently a smaller number of pixels per filopodium width, but the reliability and accuracy of segmentation are reduced, such that segmentation is problematic when several filopodia are near each other.

Because filopodia are thin protrusions, eroding the image mask that demarcates the total cell area readily removes them from the total cell mask (Fig. 1 C). Subsequent dilation re-expands the size of the cell footprint, and the subtraction of this image from the original thresholded image leaves the mask of protrusions alone. The image can thus be partitioned into separate compartments of cell body and protrusions. This procedure is similar to that used by the previously developed filopodia detection tools FiloDetect and ADAPT (Nilufar et al., 2013; Barry et al., 2015). The number of steps for erosion and dilation (ED) is user adjustable, as the optimal value is dependent on the morphological properties of the imaged cell type as well as imaging parameters such as pixel size and the purpose of the analysis (Fig. 1 D). Once protrusions are thus identified as structures separate from the cell body, it is necessary to assign their base and tip positions. This is required for tracking tip movement and base movement over time and for measuring protein fluorescence at the point on the cell body where the filopodium first protrudes and at the tip of the filopodium once it has formed. Filopodyan assigns the base and tip positions by annotating the positions within the mask of each protrusion that are nearest or furthest away from the cell body.

To measure extension and retraction events, filopodia need to be tracked over time. Structure identity is evaluated on the basis of (a) the time elapsed between the two recorded structures, (b) the distance between their base coordinates, (c) the distance between their tip coordinates, and (d) the overlap between their area in the two time points. Once the identity of structures over time is established, the dynamic parameters for each tracked protrusion are calculated (e.g., change in length, tip movement, and base movement).

Error-correcting capabilities

Some of the candidate structures initially detected are true hits, whereas others represent patches of higher-pixel-intensity noise near the boundary of the cell (Fig. 1 E). To distinguish between true and false hits, Filopodyan performs an automated filtering step on detected candidate structures. User-defined thresholds are used to eliminate candidates that do not satisfy required criteria, which include minimum number of frames in existence, the time of appearance, maximum length reached during the time-lapse, maximum tip movement during the time-lapse, and mean waviness. The values for these thresholds are customizable and need empirical adjustment for each application. A rapid preview visualizes which structures are retained with the currently set threshold values, helping the user to select useful thresholds for the filtering. A second round of automated tracking is then performed on filtered hits, yielding an automated reconstruction of tracked filopodia identities over time throughout the duration of the time lapse.

Errors in automated tracking can occur, for instance when filopodia move laterally, and in addition, some false positives may persist after automated filtering. For this reason, we included a module for manual editing of the automatically reconstructed tracks in our plugin workflow. The user can inspect the

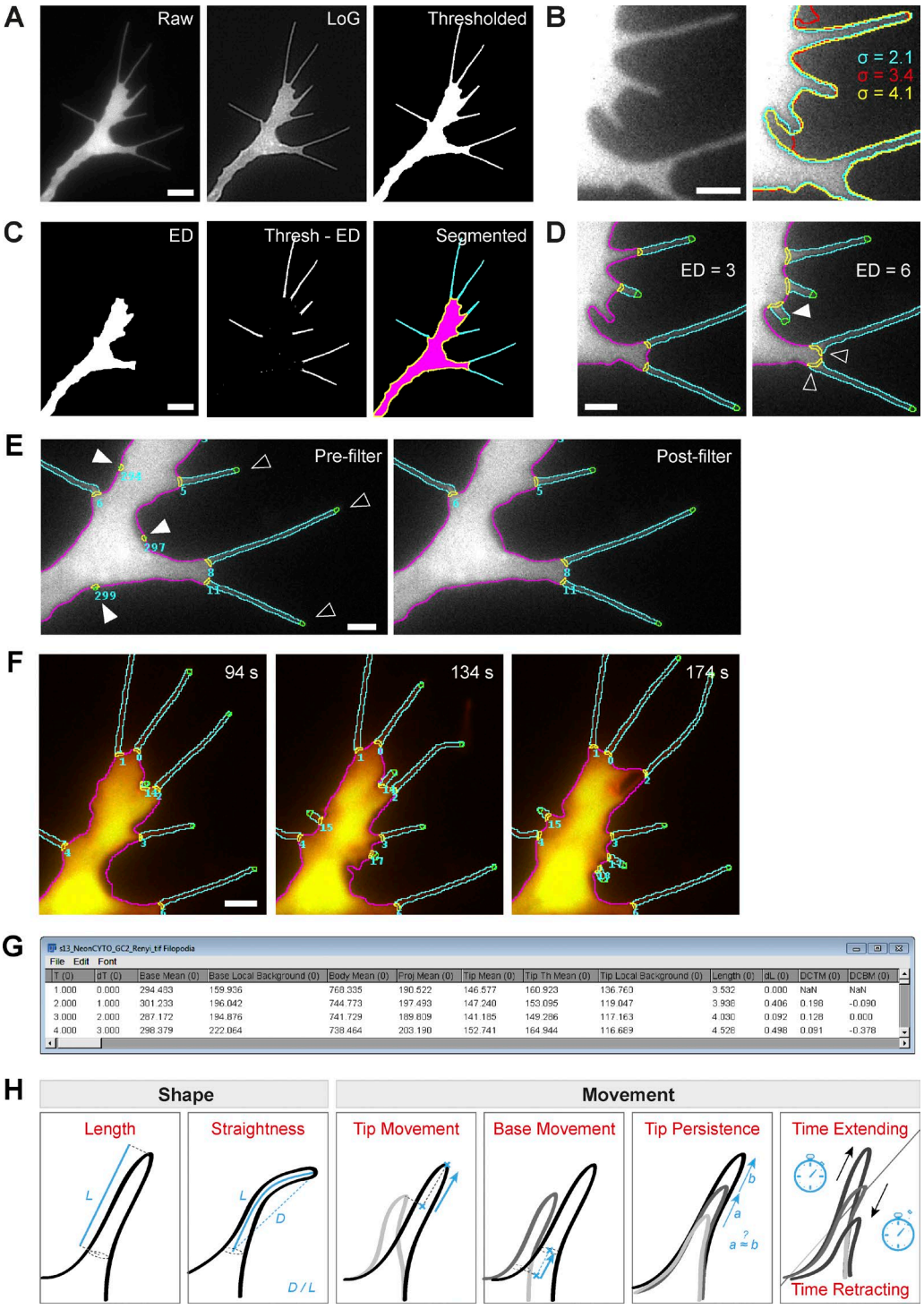

Figure 1. **Filopodyan, a highly customizable pipeline for detection, tracking, and analysis of protrusions in time-lapse datasets.** (A) Image of a *Xenopus* retinal ganglion cell growth cone with filopodia (left) is processed with a Laplacian of Gaussian (LoG) filter for edge contrast enhancement (middle) and binarized with a chosen threshold method (right). (B) Parameters for boundary mapping are customizable; colored lines show the different cell boundaries detected by using three different values of LoG σ with the Renyi entropy thresholding method. (C) Iterative erosion and dilation (ED) of the thresholded mask (from A, right) removes protrusions (left), and the difference between these two masks yields a mask with protrusions alone (center), leading to a fully segmented image (right; protrusions in cyan, growth cone body in magenta, and its boundary in yellow). (D) The cutoff threshold for segmenting protrusions is fully user customizable by adjusting the number of ED operations. The two panels illustrate the difference upon changing the ED number from 3 to 6, showing additional protrusions (white arrowhead) and shifted position of their bases (black arrowheads). (E) Automated filtering removes false hits that do not satisfy user-defined selection criteria. Detected candidate protrusions include true (black arrowheads) as well as erroneous (white arrowheads) annotations that are removed by the filter. Any false hits that escape automated filtering and incorrect tracking can be corrected manually. (F) A time series of images segmented into body (magenta), protrusions (cyan), their bases (orange), and tips (green). (G) Output tables contain the measurements at each time point (row) of protrusion shape, movement, fluorescence, and coordinates (column) for all detected protrusions (column sections). (H) Descriptive properties of filopodia extracted by Filopodyan plugin and the downstream analysis scripts include length, straightness, direction-corrected measures of tip movement and base movement, tip persistence, and the time spent extending, retracting, or stalling. Bars: (A and C) 5 µm; (B and D–F) 2 µm.

reconstruction at each time point and reject candidate structures in individual time points or across the entire time-lapse. The user can also correct errors in automated identity tracking by reassigning the identity of structures or creating identity links between different tracks.

Output parameters

Filopodyan outputs a fully segmented time-lapse with separate regions of interest (ROIs) demarcating the body, protrusion, base, and tip segments (Video 1 and Fig. 1 F), and it produces data tables containing the measured properties of each identified structure at each time point, as well as their coordinates and the corresponding fluorescence measurements (Fig. 1 G).

The directly measured morphodynamic parameters of filopodia in the Filopodyan data table are length (calculated from the perimeter value, with corrections applied for the width at the base and curvature at the tip), change in length between successive time points, tip movement from previous time point (corrected for lateral filopodium movement), and base movement from previous time point (also corrected for lateral movement; Fig. 1 H). Further filopodium properties are derived from these first-order parameters by downstream R scripts, including the persistence (autocorrelation) of tip movement, the proportion of time that the tip spends extending, retracting, or stalling and similarly the proportion of time that the base spends invading, retracting, or in a stable state. Thresholds for extension or retraction are adjustable according to the application; in our case, if mean tip movement over a time window of 10 s exceeded 32.5 nm/s (equivalent to one pixel width per time point at the imaging parameters we used), the tip was assigned to the extending state at that time point, and if it was below −32.5 nm/s, the tip was assigned to the retracting state. Equally, base movement was assigned to invading state if its mean movement over 10 s exceeded 32.5 nm/s and to retracting state if it was below −32.5 nm/s. Rolling mean (smoothing across five successive time points) was applied to the measurements of tip and base movement to reduce noise.

To verify the quality of segmentation, we compared filopodium lengths as determined by manual line tracing to lengths of the same structures as computed by Filopodyan (Fig. S1 A), revealing good correlation between the lengths of filopodia in the same time-lapse measured manually or with Filopodyan (n = 186 measurements; Pearson R = 0.97).

Robust filopodia segmentation, tracking, and measurement across cell types

We developed Filopodyan for the growth cones in *Xenopus laevis* RGC axons (Fig. 2 A and Video 1), a model system where the important role of filopodia for guidance and branching has been previously characterized in vivo (Chien et al., 1993; Dwivedy et al., 2007). We have additionally tested Filopodyan in several cell types in the developing *Drosophila* embryo because of the importance of this genetic model system. A combination of automated detection with some manual editing enables accurate detection of filopodia in *Drosophila* tracheal cells and in epithelial border cells during dorsal closure in vivo (Fig. 2, B and C; and Videos 2 and 3).

Induced pluripotent stem cell (iPSC)–derived human cortical neurons are an important model for studying neurodevelopmental and neurodegenerative conditions, including Down's syndrome and Alzheimer's disease (Shi et al., 2012). Dendrites of cortical neurons exhibit dynamic filopodia, which are precursors of dendritic spines (Hotulainen and Hoogenraad, 2010)

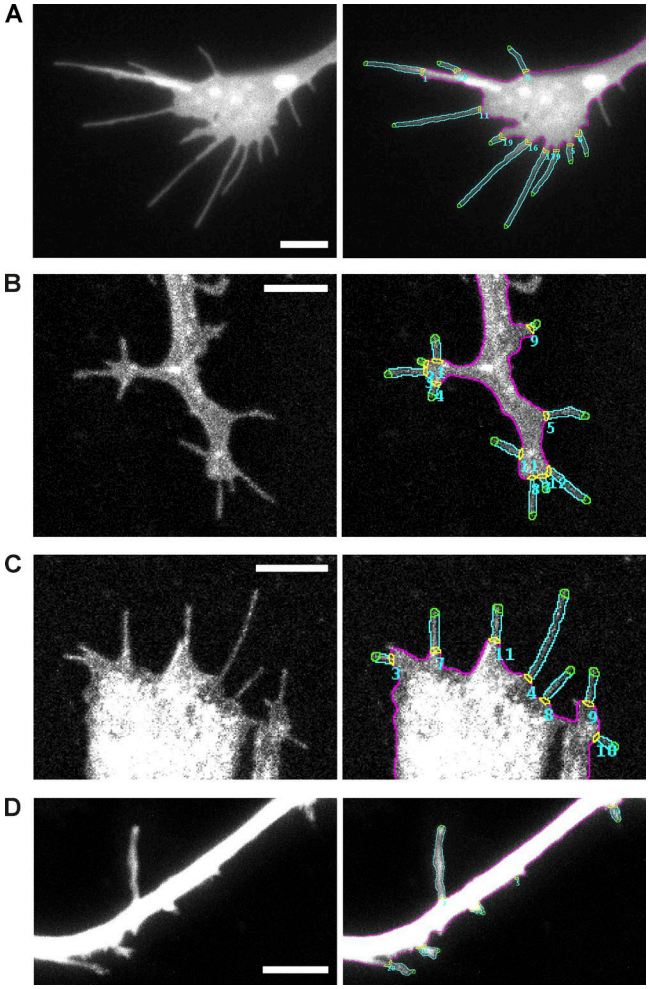

Figure 2. **Filopodyan detects and accurately segments filopodia from a variety of different cell types in vitro and in vivo.** (A) Growth cone from *Xenopus* retinal ganglion cell axons in culture, expressing GAP-RFP (a single time point from Video 1). (B) Tracheal cells in a *Drosophila* embryo expressing *btl-Gal4 UAS-Cherry-CAAX* (a single time point from Video 2). (C) Leading edge cells during dorsal closure in a *Drosophila* embryo expressing *en-Gal4 UAS-cd8mCherry* (a single time point from Video 3). (D) Human iPSC–derived cortical neurons in culture expressing cytoplasmic mNeonGreen (a single time point from Video 4). Bars, 5 µm.

and, as such, are an important structure relevant for the development of stable synapses that underlie learning and memory (Xu et al., 2009; Yang et al., 2009). We imaged the dendrites of human iPSC-derived cortical neurons in culture using two-photon microscopy and demonstrate that Filopodyan readily segments dendritic filopodia in stack projections (Fig. 2 D and Video 4). Exceptions to the versatility of Filopodyan are cell types with a very high density of filopodia and a high prevalence of filopodial crossing. In principle, this can be resolved to some extent by removing selected filopodia in the manual editing step, but other software is likely to be more suitable in these cases. Other limitations of the software include its inability to handle branching and looping events.

High-throughput extraction of filopodial features yields a content-rich dataset of filopodial dynamics from RGC growth cones

We used Filopodyan to generate a descriptive dataset of filopodial properties in *Xenopus* RGC growth cones. We analyzed

filopodia in time-lapse videos of 19 growth cones, each video lasting 4 min and captured at the frame rate of 2 s/frame. We carefully curated the automated reconstructions by manually verifying each reconstructed filopodium at each time point and rejecting inaccurate segmentations (spurious detections of noise near the growth cone boundary, as well as filopodia branching, looping, or projecting from the axon shaft).

The properties of the manually curated dataset of 160 growth cone filopodia are summarized in Table S1 and Fig. 3 A. These measurements are similar to previously reported filopodia measurements. Filopodium lengths were 8.0 ± 4.8 µm (mean ± SD; maximum length during time-lapse) and 5.6 ± 3.9 µm (mean length during time-lapse), which compares to similar measurements for filopodia in *Xenopus* RGC growth cones in vivo (5.6 µm; Chen et al., 2006; Atkinson-Leadbeater et al., 2016). Mean filopodium lengths of 7.8 µm and 7.2 µm have been reported in chick RGCs (Gehler et al., 2004) and 7.7 ± 3.6 µm in mouse dorsal root ganglion growth cones (McConnell et al., 2016). Our measured filopodial extension rate of 66 ± 26 nm/s (mean ± SD of the median extension rate per filopodium) is similar to previously reported rates in mouse superior cervical ganglion neurons (55 nm/s; Brown and Bridgman, 2003), in dorsal root ganglion neurons (59 ± 3 nm/s; McConnell et al., 2016), and in *Drosophila* primary neurons (87 nm/s; Sánchez-Soriano et al., 2010).

Manual curation is a time-intensive procedure that is prone to introducing subjective errors or human inconsistency. We thus tested how much the fidelity of reconstruction is preserved by relying only on the automated filtering step without human editing. This approach is potentially error prone, as there is no mechanism to correct errors obvious to the human eye. However, when analyzing aggregate summary data from this dataset, we found that the results were mostly comparable to the results obtained after careful user curation (Fig. 3 B; Table S1; and Fig. S1, B–I): out of 13 parameters, the only parameter significantly different between the two analyses was filopodium length (6.6 ± 4.8 µm max length in batch mode, 8.0 ± 4.8 µm in manually curated dataset, mean ± SD, Holm-adjusted Mann–Whitney P = 0.011; Table S1 and Fig. S1 B). In comparison to the manually curated dataset, which took 6 h of user input to generate (verifying the accuracy of reconstruction for >160 structures in 121 time points), the fully automated dataset was generated in 15 min using batch mode with no further human input. Thus, when image quality is sufficiently high, Filopodyan is suitable for use in rapid high-throughput characterization and phenotyping of filopodial dynamics in large datasets.

Each filopodium is characterized by a set of values describing its dynamic behavior across the entire time-lapse (maximum length reached, straightness at maximum length, median rate of extension while extending, time spent extending, etc.), numbers that together provide a summary of its morphodynamic state throughout the time-lapse. To gain new insight into the relationships between these parameters, we generated correlation matrices to mine for significant correlations (Fig. 3 C). The parameter that most strongly correlated with maximum length reached by a filopodium was its persistence of tip movement (Spearman $\rho = 0.49$, Holm-adjusted $P = 1.24 \times 10^{-8}$; Fig. 3 D). The rate of tip extension also positively correlated with maximum length ($\rho = 0.40$, $P = 2.02 \times 10^{-4}$); this agrees with the intuitive understanding that those filopodia that extend faster and whose tips display higher persistence of movement reach greater lengths. Also notably strong were the correlations indicating that filopodia with faster-extending tips spend more time extending ($\rho = 0.52$, $P = 6.53 \times 10^{-8}$) and less time stalling ($\rho = -0.54$, $P = 1.11 \times 10^{-8}$; Fig. 3 E).

Some filopodia originate by forward extension (tip-driven formation), whereas others are formed mostly as a result of lamellipodium retraction (base-driven formation), with a continuum of states between the extremes. We asked whether these formation mechanisms affected the subsequent properties later in their lifetimes. In our dataset of *Xenopus* RGC filopodia, the filopodia initiating with a greater tip extension rate during the first 20 s of their existence ("initial tip movement") reached longer maximum lengths (Fig. 3 F; Spearman $\rho = 0.49$, Holm-adjusted $P = 0.0283$), even though the initial extension did not strongly correlate with the median tip extension rate later in life ($\rho = 0.44$, $P = 0.3$). For initial base movement, no correlations with other parameters below the significance threshold of $\alpha = 0.05$ were detected (Fig. 3 F).

We next asked whether filopodia that form without tip protrusion can later extend their tips. A third of filopodia in our dataset began their life with initial tip movement below the tip extension threshold ("nonprotrusive" formation, 17/45 filopodia; Fig. S2 A). We plotted direction-corrected vector measures of tip movement, base movement, and length against time to reveal the how much the changes in filopodium length are a consequence of tip movement or base movement (Fig. S2 B shows one example from protrusive and nonprotrusive classes). As expected, protrusive filopodia later extend their tips, and furthermore, nonprotrusive filopodia were also able to sustain a tip extension later in their lifetime (Fig. S2 C). This observation is consistent with the idea that various finger-shaped protrusions (filopodia and retraction fibers) do not occupy rigid categories but instead exist within dynamically interconvertible states (Svitkina et al., 2003). Nonprotrusive filopodia attained lower length overall (Fig. S2 C, right), as expected from correlation between length and the rate of initial tip extension (Fig. 3 F).

Predicting base position before filopodia formation

To address the question of the timing of recruitment of various proteins during filopodia formation, we sought to quantify fluorescence at initiation sites on the membrane before projection of nascent filopodia. To do this, we equipped Filopodyan with a feature to map predicted base positions of future filopodia in the time points preceding their formation. For each newly formed filopodium, Filopodyan maps the XYT coordinates of the point of origin (during the first time point of its existence), and in the time points preceding its formation, the position of the future filopodium base is projected onto the edge-proximal area, thus measuring the fluorescence closest to the base of the future filopodium, to the best approximation (Fig. 4 A). This can be extended for a user-defined number of time points into the past from the moment of origin.

Given the known functional importance of ENA/VASP proteins to filopodia formation in the *Xenopus* RGCs, we asked when in the life cycle of filopodia protrusion they are recruited to growth cone filopodia. VASP has previously been reported to localize to the leading edge before filopodium formation (Svitkina et al., 2003; Disanza et al., 2013). We analyzed the preinitiation base fluorescence in a time-lapse series of growth cones expressing mNeonGreen-ENA or mNeonGreen-VASP. The expression of mNeonGreen-ENA had no significant effect on length, straightness, median rates of tip extension and retraction,

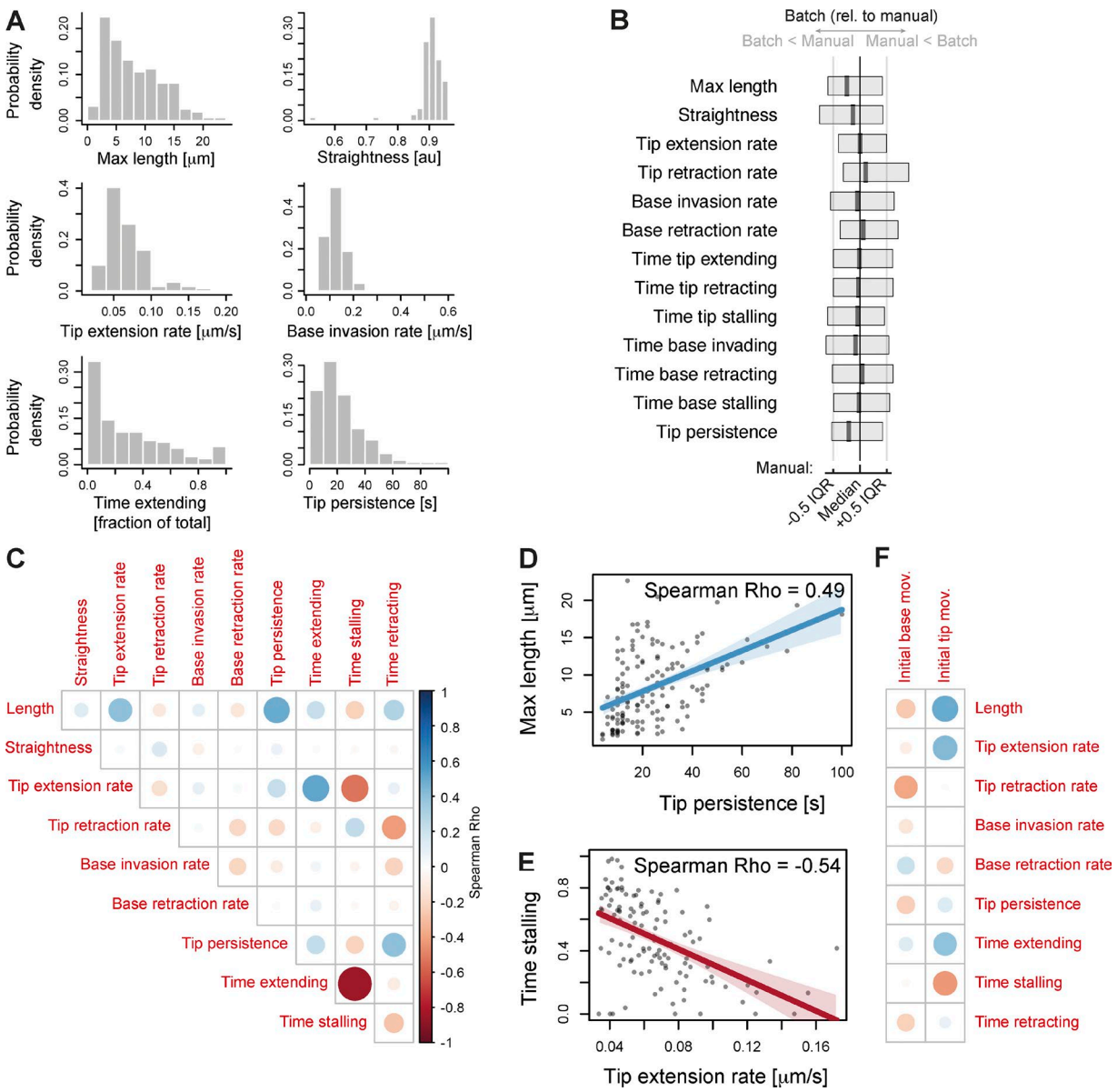

Figure 3. **Correlations between parameters of filopodial dynamics.** (A) Properties of *Xenopus* RGC growth cone filopodia from a manually curated dataset of (n = 160 filopodia and N = 19 neurons). Distribution histograms are shown for selected parameters: maximum length reached during time-lapse, straightness at maximum length, median rate of tip extension during the time-lapse, median rate of base invasion during the time-lapse, proportion of time spent in extending state, and tip persistence; see full description in Materials and methods. Descriptive statistics for these and all other parameters are in Table S1. (B) Comparison of the filopodia phenotype between two analyses of the same dataset: the manually curated analysis and fully automated batch analysis. For each parameter, the normalized boxplot represents the difference of the batch analysis relative to the manual analysis; black and gray vertical lines represent the median and interquartile range of the manually curated dataset for each parameter. Boxes and thick vertical lines represent the interquartile ranges and medians of each parameter for the fully automated (batch) dataset. Full descriptive statistics are in Table S1. (C) Correlation matrix between parameters describing filopodium shape and movement in a dataset of *Xenopus* RGC growth cone filopodia (n = 160) expressing GAP-RFP and mNeonGreen. Color scaling indicates the sign of correlation (blue to red for positive to negative); circle size indicates correlation strength. (D) Positive correlation between tip persistence of a filopodium and its maximum reached length. (E) Negative correlation between the median rate of tip extension of a filopodium and its proportion of time spent stalling. (F) Correlation matrix visualizing the correlations between the initial movement of the filopodial tips and bases (in the first 20 s after their initial appearance) with other filopodial properties in subsequent time points (after initial 20 s). IQR, interquartile range.

median rates of base invasion and retraction, tip persistence, or the proportion of time the tip spent extending, retracting, or stalling (Table S1 and Fig. 4 H; n = 59 [control] and n = 99 [ENA] filopodia from N = 7 growth cones in each condition). mNeonGreen-VASP–expressing filopodia showed a 14% reduction in the median rate of tip extension (Table S1 and Fig. 4 I; n = 55 [control] and n = 90 [VASP] from N = 8 [control] and N = 11 [VASP] growth cones; Mann–Whitney Holm-adjusted P = 0.044) but displayed no significant effect on other measured parameters. Thus, the filopodia in mNeonGreen-ENA– and VASP-expressing growth cones were largely similar to filopodia in the control, mNeonGreen–expressing growth cones.

We observed that mNeonGreen-ENA localizes to the leading edge of advancing lamellipodia immediately preceding filopodia formation (Fig. 4, B and C; and Video 5). In newly detected protrusions (n = 52) from eight growth cones (an exam-

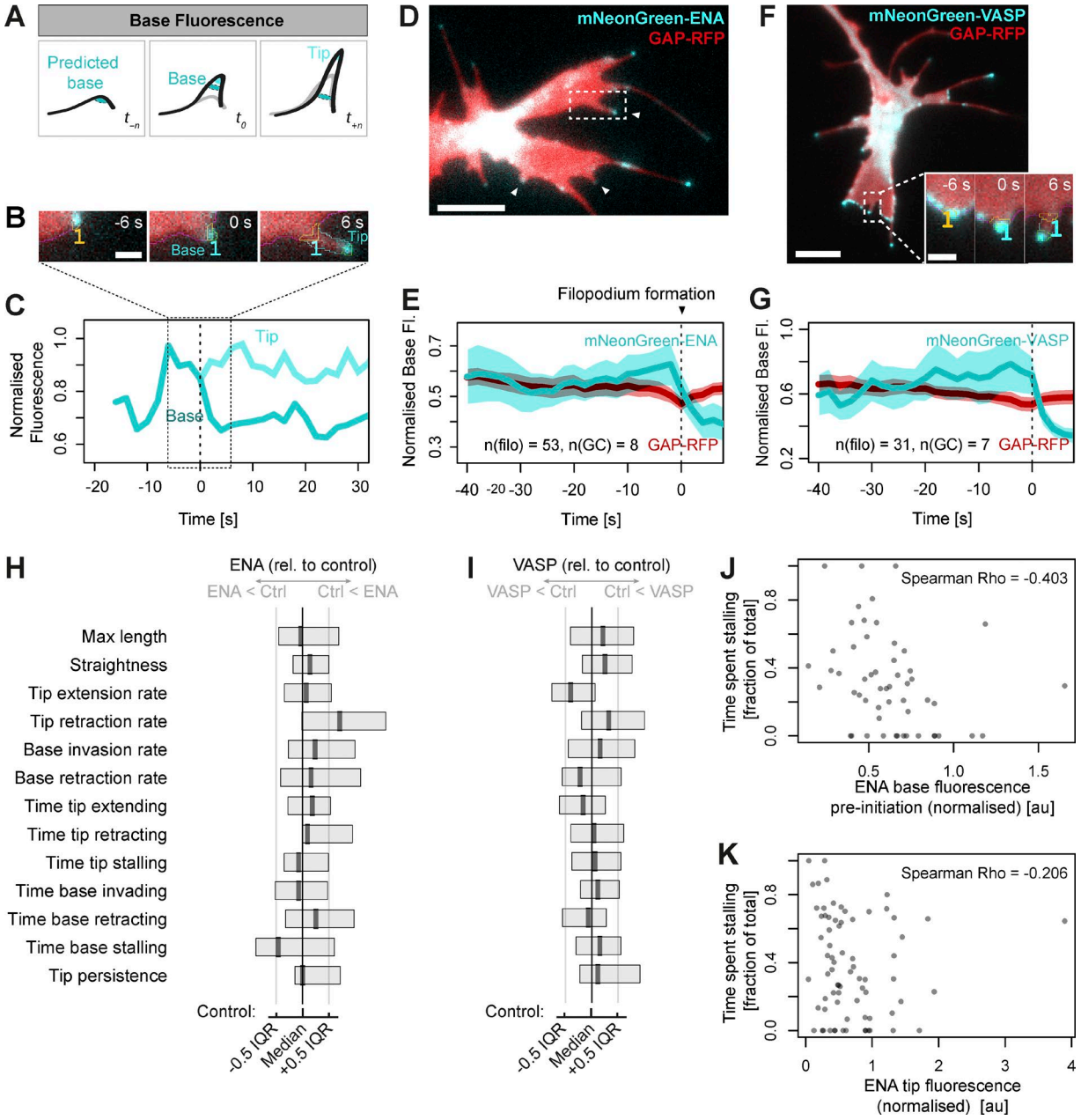

Figure 4. **Predicted filopodium base position enables the measurement of protein recruitment before filopodium formation.** (A) Measurements of fluorescence are taken at bases and tips of filopodia during formation (t_0) and throughout their lifespan (t_n). In addition, fluorescence at the boundary is recorded at the position closest to the site of nascent filopodium formation for a defined number of frames before initiation (t_{-n}). (B) Example filopodium from a growth cone (shown in D) expressing mNeonGreen-ENA and GAP-RFP, illustrating the accumulation of ENA signal at the advancing lamellipodial edge before and during filopodium formation (orange outlined region in B). (C) Quantification of mNeonGreen-ENA fluorescence in the (predicted) base area (orange) and in the tip (green) of the single example filopodium from B. Base fluorescence and thresholded tip fluorescence are normalized against growth cone body fluorescence. After the moment of formation (t_0) the enhanced fluorescence signal travels onwards with the moving filopodium tip while dropping at the base. (D) A still image from a time-lapse (Video 5) of a growth cone showing three filopodia during formation all exhibiting enriched levels of ENA fluorescence signal (arrowheads). (E) Normalized base fluorescence (mean and 95% confidence interval) at newly forming filopodia (n = 53, from eight growth cones) expressing mNeonGreen-ENA (cyan), showing accumulation at the site of future filopodium initiation in the time points immediately preceding its formation; this accumulation is not observed for the membrane marker GAP-RFP (red). (F) A still image from a time-lapse (Video 6) of a growth cone expressing mNeonGreen-VASP during the moment of filopodium formation (inset). (G) Normalized base fluorescence at newly forming filopodia in growth cones expressing mNeonGreen-VASP (n = 31, from seven growth cones), showing an increase in fluorescence before initiation. (H) Summary of filopodia properties in neurons expressing mNeonGreen-ENA, compared with mNeonGreen control. (I) Summary of filopodia properties in neurons expressing mNeonGreen-VASP, compared with mNeonGreen control. See Table S1 for full information. (J) Relationship between normalized mNeonGreen-ENA fluorescence at predicted base position before filopodium formation and the proportion of time the filopodium subsequently spent stalling, showing negative correlation. (K) Normalized mNeonGreen-ENA fluorescence at the tip and the proportion of time spent stalling, not recapitulating the negative correlation seen with predicted base fluorescence shown in J. Bars: (main panels) 5 μm; (inset) 1 μm.

ple in Fig. 4 D shows three newly formed or forming filopodia), we observed on average a slow and modest gradual increase in membrane-proximal fluorescence at sites of future filopodia initiation (Fig. 4 E). Base fluorescence of ENA peaked at 2 s before formation, followed by a decrease upon filopodia formation as the tips move away from the base region. Such increase before formation was not observed for a membrane-localizing control construct (GAP-RFP), indicating that the observed peak was not a consequence of nonspecific membrane localization. A similar pattern of accumulation before filopodia formation was observed for mNeonGreen-VASP (Fig. 4, F–G; and Videos 6 and 7; Svitkina et al., 2003).

There is variability between filopodia in the extent to which such increase in fluorescence signal is observed before initiation. We wondered whether the extent of ENA or VASP accumulation before formation affects the subsequent properties of filopodia. To address this question, we looked at the correlation between ENA or VASP intensity before formation and each of the measured properties for all filopodia in our dataset. (The accuracy of predicted base positioning diminishes with time further away from the moment of formation; for increased accuracy, we only used the last 6 s before formation, which also coincides with the time where ENA and VASP accumulation was greatest on average.) Significant negative correlation was found with the proportion of time spent stalling; filopodia with stronger ENA fluorescence before formation spent less time stalling (Fig. 4 J). It is possible that filopodia that start with a surge of ENA end up with higher level of ENA overall, therefore giving rise to more movement. However, the correlation between ENA intensity at the tip and time spent stalling has a lower overall correlation than base intensity with time spent stalling (Fig. 4 K). Thus, we find that that those filopodia that start their lives with a surge of ENA accumulation spend more time in a moving state than those with less ENA accumulation at the membrane immediately before formation, without differing in other parameters. No significant correlations between VASP accumulation before filopodia formation and parameters of filopodia dynamics were detected (n = 31, α = 0.05, with Holm adjustment for multiple comparisons).

Measuring protein accumulation at the tip during filopodia extension

In nascent filopodia, actin polymerization at the distal end propels the extension of the filopodia tips, driven by actin-regulatory factors that localize to the tip (referred to as the "tip complex"; Mallavarapu and Mitchison, 1999; Applewhite et al., 2007). Our initial reconstructions of the cell boundary based on the membrane signal did not always reach all the way to the tips, meaning that the majority of tip fluorescence signal was sometimes located just outside the annotated filopodia areas (Fig. 5 A). To compensate for this, we designed a refinement to tip positioning. For tip-localizing fluorescent proteins, their position can be taken into account to refine the tip coordinates positioning after they are initially assigned from the membrane marker (mapping) channel (Fig. 5 A, tip fitting). We could therefore monitor extensions and retractions of the filopodia tips in parallel with the fluorescence in those filopodia tips, indicative of the accumulation of proteins of interest. "Fragment joining," an additional method for improving accuracy of filopodia reconstruction, is also included in Filopodyan: with this option, separate object fragments are extended back to the closest point on the body boundary (Fig. 5 B, fragment joining). Filopodia frequently move in and out of plane of focus during imaging. Those events are accompanied by sudden jumps in measured tip movement, which we filter in our R scripts for downstream processing, thus eliminating out-of-focus time points from analysis. In addition, in our analyses of tip fluorescence and movement, automated reconstructions were extensively manually curated to ensure highest possible accuracy.

Different relationships between ENA tip fluorescence and filopodia properties

In lamellipodia, the accumulation of VASP at the leading edge positively correlates with leading edge speed during extension (Rottner et al., 1999). To understand how ENA and VASP accumulation acutely affect the dynamic behavior of filopodia tips, we asked how tip fluorescence relates to tip movement once filopodia have protruded from the cell body. In some filopodia, we observed a positive relationship between ENA tip fluorescence and tip movement: in those filopodia, the loss of tip fluorescence was tightly paralleled by tip retraction, and increases in tip fluorescence paralleled their regrowth (either instantaneously or with a delay; Fig. 5, C–E; and Video 8). However, this was not the case with all filopodia; there are clear instances where positive fluorescence persists while the tip is retracting (Fig. 5, F–H; and Video 9), illustrating that different filopodia within the same cell type can respond to tip accumulation of ENA in different ways.

To quantitatively assess the response of individual filopodia to ENA accumulation within their tips, we calculated for each filopodium the extent of correlation between tip fluorescence and tip movement across the entire time-lapse. Allowing for the fact that the effect of one on the other may occur with a delay, we also assessed the correlation for various levels of delay between the two quantities (time offset) using a cross-correlation function (CCF) to assess this relationship as a function of time offset for each filopodium individually (Fig. 5 I). We grouped filopodia sharing a similar relationship between tip fluorescence and movement using hierarchical clustering (Fig. 5 I). 14 out of 46 filopodia (30%) displayed a positive correlation (CCF = 0.54) between ENA tip fluorescence and movement (Fig. 5 I). To verify whether this was a genuine effect rather than an artifact of the clustering algorithm, we randomized the order of tip movement measurements in a way that preserved their autocorrelation and repeated the clustering analysis on the randomized datasets. Randomization significantly reduced the cross-correlation between fluorescence and movement of the positively correlating subcluster (bootstrap $P < 0.001$; Fig. S3, A–E). This demonstrates that the positive correlations between ENA localization and tip movement are considerably stronger than would be expected at random in a dataset where ENA localization and tip movement are decoupled from each other.

To test this observation even more rigorously we used a Monte Carlo method. We modeled each filopodium separately based on its tip fluorescence and tip movement measurements, generating 10,000 Markov chain simulations for tip fluorescence and, independently of those, 10,000 for tip movement. We recorded pairwise correlations observed between these independently generated Markov chains and compared the distribution of simulated correlation coefficients for each filopodium to the observed correlation coefficient in our real measured dataset for the same filopodium (Fig. S4). A single example illustrates a filopodium with positive correlation between tip fluorescence and movement (Fig. S4, A and B) and one example simulation

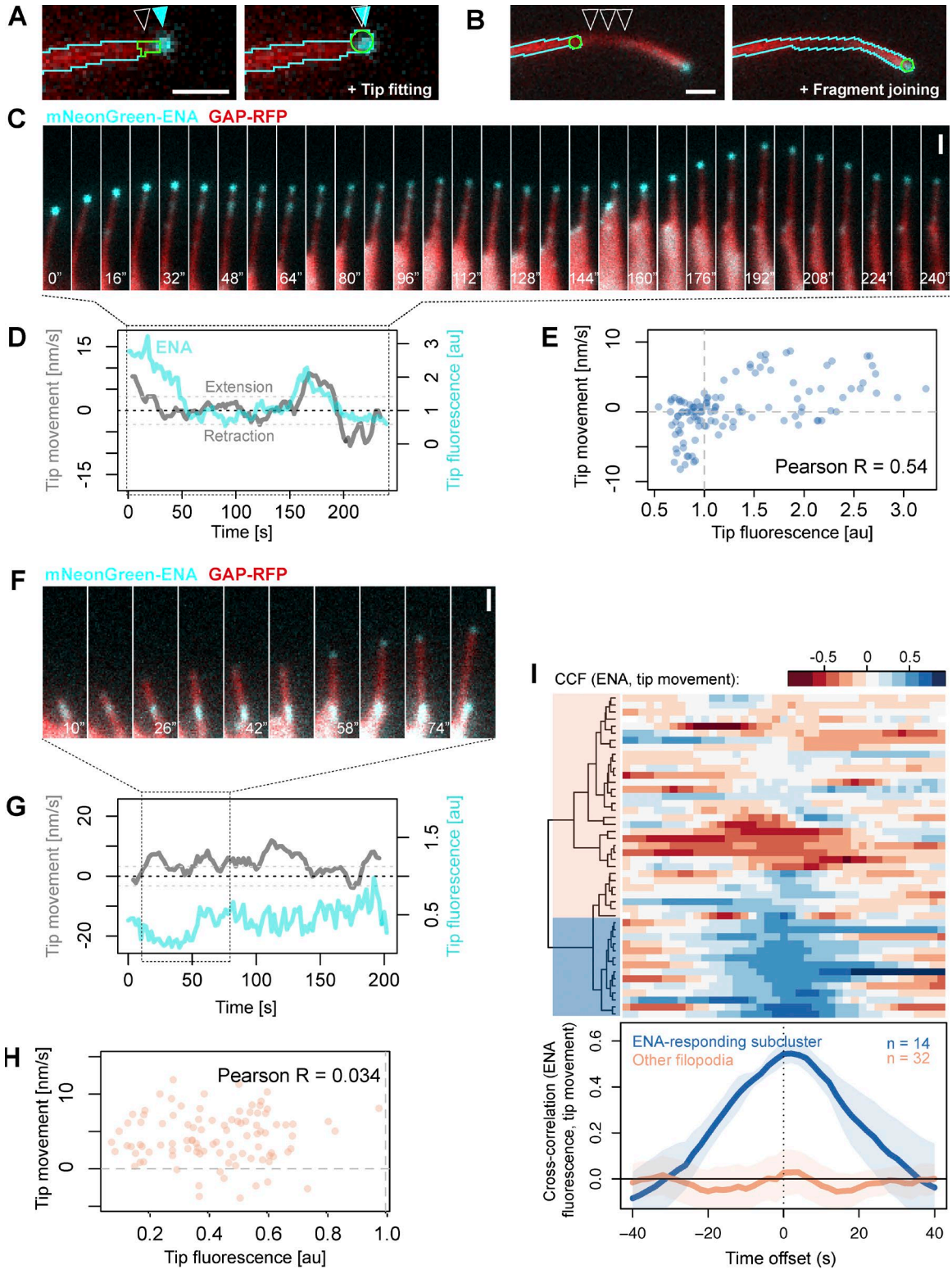

Figure 5. **Analysis of tip fluorescence and tip movement.** (A) For the purpose of quantifying fluorescence in filopodia tips, the tip fitting mode of Filopodyan searches for accumulation of fluorescence signal in the immediate vicinity of initially assigned tip positions and readjusts the assigned tip position (white arrowhead) to match the position of the fluorescence signal (cyan arrowheads). (B) Filopodyan also allows connecting disconnected fragments (e.g., caused by loss of focus; arrowheads) with the reconstructed filopodium. (C) A time-lapse series of a filopodium from *Xenopus* RGC growth cone expressing mNeonGreen-ENA (Video 8), showing enhanced forward tip movement upon increased ENA fluorescence (at 0–20 s and 160–192 s) and absence of movement or tip retraction upon reduced ENA fluorescence (40–160 s and 192–240 s). (D) Concurrent tip fluorescence (normalized to growth cone fluorescence) and tip movement (smoothed with a five-step rolling mean) measurements for the example filopodium shown in C, showing positive correlation between fluorescence and movement. Dashed gray lines at −32.5 and +32.5 nm/s represent the thresholds for retraction and extension. (E) Positive correlation between ENA tip fluorescence and tip movement across the time-lapse for the example filopodium shown in C (with no time offset). (F) An example filopodium showing lack of correlation between tip ENA accumulation and tip movement (e.g., extending without ENA enrichment during 10–34 s). See

where there is no correlation (Fig. S4, C and D). The entire set of simulations for this filopodium shows no correlation between tip movement and fluorescence, in contrast to the observed behavior (Fig. S4 E). Not a single simulation meets the correlation found in the observed data (Fig. S4 E).

The results of this analysis for each of the filopodia in the dataset showed that in 9 out of 42 filopodia, fewer than 100 in 10,000 simulations ($P < 0.01$) recapitulated the correlation observed in the real dataset (Fig. S4 F). (The observed correlation coefficients for these filopodia were all at least 2.8 SD away from the mean of the simulated correlation coefficients [Fig. S4 F].) This means that a subset of filopodia expressing mNeonGreen-ENA displayed correlations between ENA fluorescence and tip movement at levels that would be unlikely to arise at random from their fluorescence and movement properties if these quantities were fully independent of each other, even when their temporal statistics are recreated with a Markov model.

To determine whether filopodia that have the strongest positive correlation between the accumulation of ENA in their tips and tip movement differ in other properties compared with less-correlating filopodia, we selected the top correlating cluster of filopodia for further analysis (Fig. 5 I). We call these "ENA-responding" filopodia. This encompasses the possibilities that ENA accumulation influences or responds to movement or that both are influenced by a third parameter. We compared all measured morphodynamic properties of the ENA-responding filopodia compared with all other filopodia. We found no significant differences in any of those properties between ENA-responding filopodia and other filopodia (Table S1). They also did not differ in their fluorescence properties (tip fluorescence, total filopodium fluorescence, or body fluorescence; Table S1), indicating that filopodia with different ENA responsiveness did not importantly differ in their level of expression of exogenous mNeonGreen-ENA.

VASP-responding filopodia have distinct dynamic properties

Similarly, for VASP, we discovered that some filopodia show a strong positive response to VASP fluorescence accumulation in their tips, whereas others do not (Fig. 6, A–F). With hierarchical clustering according to their cross-correlation between fluorescence and movement, we identified 9 VASP-responding filopodia among our dataset of 76 (12%) that were strongly responsive to VASP accumulation in their tips (CCF = 0.80; Fig. 6 G). As for the ENA dataset described in the previous section (Figs. S3 and S4), the significance of the strength of this correlation was confirmed for VASP with randomization analysis (Fig. S3, F–J) and with Markov chain simulations (Fig. S4 G). Unlike ENA-responding filopodia, which were similar to other filopodia in all measured properties, the VASP-responding filopodia reached significantly greater maximum lengths than other filopodia, had a higher median rate of tip extension, and spent more time retracting and less time stalling, and their bases spent more time invading (Table S1 and Fig. 6, I and J). VASP-responding filopodia and filopodia not responding to exogenous mNeonGreen-VASP coexist side by side within the same growth cone (Fig. 6 H and Video 10), suggesting that this observation is not caused by differences in how different cells respond to exogenous VASP expression but rather reflects heterogeneity in the molecular properties of filopodia within a single cell.

In our analysis, subgroup allocations according to VASP responses depend on manual selection of clustering thresholds. To assess the robustness of our observations, we repeated the analysis so that a larger group of filopodia was assigned to the VASP-responding cluster ($n = 37$ out of 76 filopodia, 49%; Fig. S5 A). In this case, their collective CCF was reduced compared with the smaller subset of most strongly positively correlating filopodia, as expected (CCF = 0.6 compared with CCF = 0.8 for the smaller subset of nine filopodia) but still peaked at offset = 0 (Fig. S5 B). Importantly, the correlation was strongly significant according to the randomization analysis; 0 out of 1,000 randomizations recapitulated the observed cross-correlation given the defined cluster size (Fig. S5 C). We repeated the morphological and dynamic assessment of whether this expanded subgroup of filopodia had the same distinct properties as the smaller subgroup. Although the maximum length and mean tip extension rate were no longer significantly different between the larger VASP-responding subgroup and other filopodia, the increase in time spent retracting and the decrease in stalling time compared with the other filopodia were preserved (Table S1).

Discussion

Automated detection and analysis of filopodia

We developed Filopodyan, an open-source image analysis pipeline for automated segmentation and analysis of filopodia, which rapidly annotates and tracks large numbers of dynamic filopodia. It provides options for interactive manual correction of automated reconstructions, allowing its use even in situations when accurate segmentation of filopodia is difficult. We demonstrate that Filopodyan robustly identifies filopodia in a variety of model systems (two neuronal cell types in culture [RGC growth cones and dendritic filopodia in human cortical neurons] and two different cell types during *Drosophila* development in vivo) and across a range of imaging modes (total internal reflection fluorescence [TIRF]/highly inclined laminated optical sheet [HILO], two-photon, and conventional line-scanning confocal microscopy; Fig. 2). Filopodyan has therefore proven useful in various contexts important for the study of filopodia, and its flexible format means it is widely adaptable. Filopodyan is written in Fiji and R, and all plugin and analysis scripts are publicly available at https://github.com/gurdon-institute/Filopodyan.

In addition to measuring filopodia shape and movement, our plugin measures the fluorescence of the whole filopodium,

also Video 9. (G) Concurrent tip fluorescence and tip movement measurements for the example filopodium shown in F. (H) Absence of correlation between ENA tip fluorescence and tip movement measurements across the time-lapse for the example filopodium shown in F. (I) Cross-correlation function (CCF) between normalized ENA tip fluorescence and tip movement for each filopodium (rows) for each value of time offset (columns) between fluorescence and movement, displayed as a heatmap. Blue shows a positive correlation and red a negative correlation. Negative offset, fluorescence precedes movement; positive offset, fluorescence lags behind movement. $n = 46$ filopodia. Blue shaded block on the dendrogram indicates the subcluster of positively correlating (ENA-responding) filopodia. Line plot shows collective CCF values for each subcluster (ENA-responding filopodia and all other filopodia); lines and shading represent means ± 95% confidence intervals. Bars, 1 µm.

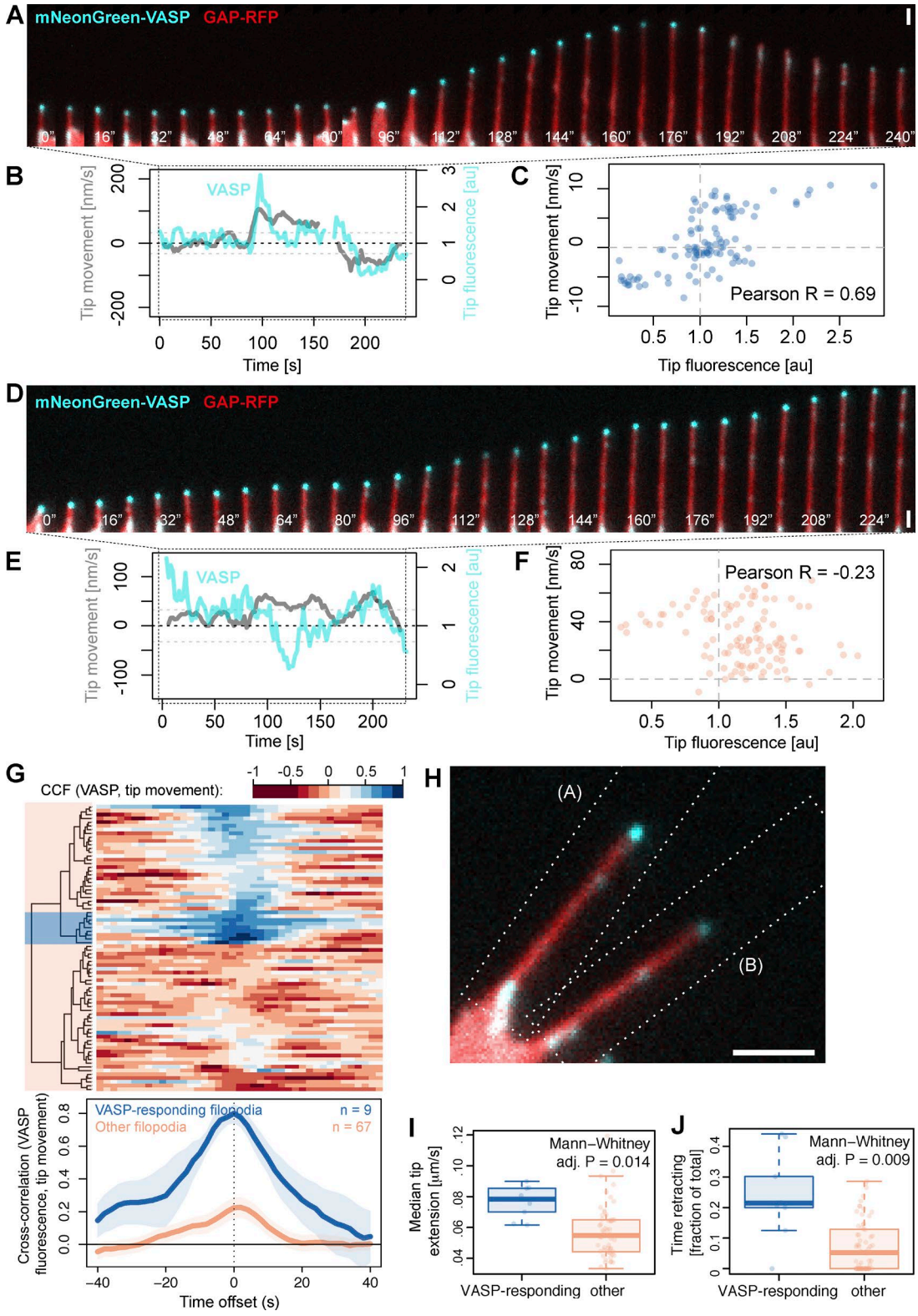

Figure 6. **Heterogeneity of filopodia responses to VASP accumulation within their tips.** (A) A filopodium from *Xenopus* RGC growth cone expressing mNeonGreen-VASP, showing a positive response to VASP accumulation within its tip (surge of forward movement from 96 s, retraction concomitant with the loss of tip fluorescence from 184 s). (B) Concurrent measurements of VASP fluorescence and tip movement for the example filopodium shown in A. (Interruption at t = 160 s represents loss of focus during those time points.) (C) Positive correlation between VASP tip fluorescence and tip movement across the time-lapse for the example filopodium shown in A (at time offset 0). (D) An example filopodium expressing mNeonGreen-VASP showing stalling at elevated levels of VASP (0–80 s) and forward tip extension during a period of reduced VASP fluorescence (112–136 s). (E) Concurrent VASP fluorescence and tip movement measurements across the time-lapse for the filopodium shown in D. (F) Absence of positive correlation between VASP fluorescence and tip movement across the time-lapse for the filopodium shown in D, at time offset 0. (G) Cross-correlation between VASP fluorescence and tip movement for each filopodium (rows) as a function of time offset (columns). n = 76 filopodia. Red shows a negative correlation and blue a positive correlation. Negative

the tip and the base, as well as the predicted base position before filopodium formation. This enables the analysis of the roles of specific proteins on the scale of seconds and micrometers, which is necessary to understand the molecular basis of filopodium growth and behavior at the relevant spatiotemporal scale of protrusive behavior.

Advantages and disadvantages of Filopodyan

Filopodyan measures filopodia fluorescence with full automation and generation of systematic large datasets of fluorescence intensity at membrane-proximal sites during formation and at the tip. Segmentation uses a membrane marker, providing an alternative to the actin signal used by FiloQuant (Jacquemet et al., 2017 *Preprint*) and CellGeo (Tsygankov et al., 2014). Filopodyan has the flexibility to allow high-throughput (batch) processing or a highly user-interactive mode that enables generation of manually curated datasets. Tip tracking and fragment joining for enhanced accuracy of measurement at filopodia tips are significant features compared with previous software. Filopodyan has wider scope than FiloDetect (Nilufar et al., 2013) and is implemented in ImageJ rather than commercial software (MATLAB). Filopodyan is more tailored for filopodia specifically compared with MATLAB-based CellGeo (Tsygankov et al., 2014) and ImageJ-based ADAPT (Barry et al., 2015), where filopodia are a subset of protrusions that are capable of being detected. FiloQuant is best suited for filopodia within 3D environments and does not incorporate protein fluorescence measurements (Jacquemet et al., 2017 *Preprint*). Saha et al. (2016) have pioneered systematic fluorescence measurement within filopodia, looking at both tip fluorescence and fluorescence along the length of the filopodium, in low throughput. Filopodyan measures the fluorescence at the membrane-localized sites of actin incorporation at both tips and bases and links this with the parameters of filopodia morphology and dynamics in large datasets, in open source format and with a user-friendly graphical user interface.

Filopodyan performs well on high-magnification, high-quality images in cell types with clearly separated filopodia, in two-dimensional time series. The way in which Filopodyan assigns the tip (furthest point away from the base at the cell body) means that branched filopodia tip positions are inaccurately assigned. Here, we manually removed such filopodia from further analysis and recommend that the automated mode of Filopodyan should not be used when branched filopodia are prominent.

The segmentation process used by Filopodyan is based on ED (similar to previous software ADAPT and FiloDetect) and is not appropriate for overlapping or looping filopodia. Different segmentation strategies, for example those used by FiloQuant (Jacquemet et al., 2017 *Preprint*), may perform better in these cases. Although filtering steps and manual editing help with cells that have overlapping, branching, or looping filopodia, Filopodyan has not been developed in such situations.

Mechanisms of filopodia initiation

A longstanding debate in filopodia formation is whether filopodia arise from and are embedded within a dynamic actin network of the lamellipodium (convergent elongation) or whether they form anew independently of the preexisting network (tip nucleation; Yang and Svitkina, 2011). It is clear that cells are capable of producing filopodia through diverse mechanisms; for instance, in fibroblasts lacking ENA/VASP proteins or the formins mDia1/mDia2, expression of either VASP or mDia2 results in overproduction of filopodia, but they have different dynamic and structural properties (Barzik et al., 2014). Similarly, during *Drosophila* dorsal closure, Enabled and Diaphanous drive the production of filopodia with distinct properties in vivo (Nowotarski et al., 2014). To understand how cells normally produce filopodia and to assess the involvement of various actin regulators during their formation, it is necessary to systematically quantify their accumulation at the membrane. This has so far only been reported in a cell-free system of filopodia-like structures on supported lipid bilayers, suggesting a hierarchical order of protein accumulation to newly forming filopodia (Lee et al., 2010). We used Filopodyan to quantify the enrichment of ENA and VASP at the membrane before filopodia initiation and protrusion in growth cones of RGC axons (Fig. 4) as a first step toward characterization of the relative timing of recruitment of actin-regulatory and membrane-binding proteins to filopodia initiation sites. Although *Xenopus* RGCs offer a powerful context for studying filopodia of characterized function, one limitation is the need for exogenous expression of labeled proteins. Importantly, the expression of mNeonGreen-ENA or VASP did not substantially alter the morphodynamic properties of filopodia (Fig. 4, H and I; and Table S1), indicating that the level of exogenous protein expression was not disruptive to filopodia at the levels we have used. Emergent gene editing technology offers a way to label proteins endogenously and further refine such quantitative approaches.

Molecular mechanisms of filopodia tip extension

We developed a method to quantify the relationship between tip fluorescence and filopodia protrusion by cross-correlation and clustering analysis, similar to previous approaches used for lamellipodia (Machacek et al., 2009; Barry et al., 2015; Lee et al., 2015). We show that the accumulation of ENA and VASP within filopodia tips can positively correlate with their extension (Figs. 5 and 6). This effect is limited to a subset of filopodia, whereas the extension of other filopodia appears independent of the level of ENA or VASP fluorescence in their tips. Although we cannot exclude a potential contribution of endogenous unlabeled ENA or VASP, growth could also be under the control of other actin regulatory proteins, such as formins. Although ENA-responding filopodia harbor similar properties to other filopodia, the most positively VASP-responding filopodia grow to greater lengths, exhibit faster tip extension, and spend more time in a dynamic state than other filopodia. The

offset, fluorescence leads before movement; positive offset, fluorescence lags behind movement. Blue shaded block over the dendrogram represents most strongly positively correlating (VASP-responding) filopodia, and red indicates all other filopodia. (H) The VASP-responding and other filopodia from A and D occupy adjacent positions in the same growth cone. Dashed rectangles indicate crop regions used for the kymographs in A and D. (A still image from Video 10.) (I and J) Filopodia from the VASP-responsive subcluster have a higher rate of tip extension (I) and spend more time retracting (J) than other filopodia. Tukey box plots (box: first and third quartile; upper and lower whiskers: within 1.5 interquartile range of the upper and lower quartile, respectively); p-values are provided for Mann–Whitney test after Holm correction for multiple comparisons. Full information on subcluster properties is in Table S1. Bars: (A and D) 1 µm; (H) 2 µm.

filopodia in the larger subgroup showing VASP-responsiveness (approximately half) also spend more time retracting and less time stalling than the remaining filopodia. It may be the filopodia with lower correlation between VASP and tip movement are responding to a different subset of actin regulators. To test whether the combination of actin regulators at the tip is a more relevant measure than any single one, labeling of multiple proteins at the same time and combining with molecular interventions will be needed.

In our cross-correlation analysis of tip fluorescence and tip movement, we worked under the assumption that filopodia occupy a single state of responsiveness throughout their lifetime. However, in time series of individual filopodia, we have observed cases where filopodia not responding to VASP fluorescence seemed to switch to a responding state (e.g., Fig. 6 E, after t = 170 s). Longer time periods of data acquisition are needed to determine whether such switching is a common feature of filopodia.

Filopodia in brain development

During their navigation in vivo, axons respond to several extracellular signals. Many of these signals have been shown to affect filopodia formation, including glutamate (Zheng et al., 1996) and the classical guidance cues Netrin-1 (Lebrand et al., 2004) and Slit (McConnell et al., 2016). Differences in the molecular mechanisms and morphological and dynamic parameters are likely tuned by the complex signaling environments in the brain. This in turn could dictate microtubule capture and stabilization of filopodia that support neurite formation (Geraldo et al., 2008), growth cone turning (McConnell et al., 2016), or the formation of new branches in search of synaptic partners (Kalil and Dent, 2014). Filopodyan thus provides a tool to link molecular regulation of filopodia to the cellular dynamics of brain development.

Materials and methods

Animals

This research has been regulated under the Animals (Scientific Procedures) Act 1986 Amendment Regulations 2012 following ethical review by the University of Cambridge Animal Welfare and Ethical Review Body.

Constructs and capped RNA synthesis

pCS2-mNeonGreen-FA was generated by amplifying mNeonGreen (Shaner et al., 2013) from pNCS-mNeonGreen (supplied by Allele Biotechnology and Pharmaceuticals) with primers containing EcoRI and FseI sites (forward: 5′-GCATGAATTCACCATGGTGAGCAAGG-3′, reverse: 5′-GATCGGCCGGCCTCTTGTACAGCTCGTCC-3′), subsequently cloning the PCR product into pCS2-His-FA; pCS2-His-FA was constructed by digesting pCS2-FA with FseI and AscI and annealing 5′-phosphorylated linker oligos containing His_6, EcoRI, and FseI sites (forward: 5′-TTACCATGCATCATCATCATCATCACGAATTCAGGCCGGCCTGAGG-3′, reverse: 5′-CGCGCCTCAGGCCGGCCTGAATTCGTGATGATGATGATGATGCATGGTAACCGG-3′). mNeonGreen-ENA was generated by amplifying the *Xenopus laevis* ENA sequence (BC073107) from pCMV-Sport 6-ENA (Open Biosystems) using primers containing FseI and AscI sites (forward: 5′-GCATGGCCGGCCACCATGAGTGAACAGAGCATC-3′, reverse: 5′-GGCGCGCCCTATGCGCTGTTTG-3′) and cloning into pCS2-mNeonGreen-FA using FseI and AscI. mNeonGreen-VASP was generated by amplifying the *X. laevis* VASP sequence (BC077932.1) from His-mCherry-VASP (Lee et al., 2010) with primers containing FseI and AscI sites (forward: 5′-GCATGGCCGGCCACCATGAGTGAGACAGC-3′, reverse: 5′-GGCGCGCCGGTCAAGGAGTACCC-3′), subsequently cloned into pCS2-mNeonGreen-FA using FseI and AscI. GAP-RFP (Lin et al., 2009) was a gift from the Holt laboratory. For capped RNA synthesis, these plasmids were linearized with NotI and transcribed in vitro using SP6 mMessage mMachine (Ambion) following the manufacturer's instructions and diluted in RNase-free water.

Xenopus RGC growth cones

Xenopus embryos were obtained by in vitro fertilization and reared in 0.1× modified Barth's saline at temperatures ranging from 14°C to 18°C. Developmental stages were determined according to Nieuwkoop and Faber (1967). At embryonic stages 26 to 28, RNA was introduced into eye primordia by eye electroporation at 0.5 µg/µl per construct as previously described (Falk et al., 2007). In brief, embryos were placed inside custom-made Sylgard electroporation chambers with platinum electrodes placed either side of the embryo. RNA was delivered by microinjection to a site medial to eye primordia, followed by the application of eight 18-mV pulses of 50-ms duration, separated by 1-s intervals. Eye explants of stage 35 to 36 embryos were cultured as previously described (Leung and Holt, 2008) on 35-mm glass-bottom culture dishes (Ibidi) coated with 10 µg/ml poly-L-lysine overnight (Sigma) and with 10 µg/ml laminin (Sigma) for 3 to 5 h (Leung and Holt, 2008). Eye explants were cultured in phenol red–free L-15 culture media (Invitrogen), and imaging was conducted 19 to 23 h after plating. Imaging of retinal explants was conducted in the same culture media with HILO illumination (Tokunaga et al., 2008) on a custom-made TIRF setup based on a Nikon Eclipse Ti-E inverted microscope equipped with an iLas2 illuminator (Roper Scientific), a CMOS camera (Hamamatsu Flash 4), and an Optosplit beam splitter (Cairn Research). Images were acquired in a single z plane at a rate of 2 s per time point with a 100× 1.49 NA oil immersion objective at room temperature using MetaMorph software (Molecular Devices). Only growth cones clearly separated from other axons were chosen for imaging.

Drosophila stocks and embryo live imaging

Flies were raised at room temperature on standard fly food. The following fly stocks were obtained from the Bloomington *Drosophila* Stock Center: {en2.4-Gal4}e16E (BL30564); w; P{UAS-mCD8.ChRFP} (BL 27392). w; btl-Gal4 UAS-CAAX-mCherry/TM6b was obtained from S. Hayashi (RIKEN Center for Developmental Biology, Kobe, Japan). Genotypes used for live imaging were *;en-Gal4/CyO; UAS-cd-8mCherry* for leading edge cells during dorsal closure and *btl-Gal4 UAS-Cherry-CAAX/TM6b* for terminal tracheal cells. After egg-laying overnight at 25°C, embryos were dechorionated in thin bleach for 1 min and mounted on a coverslip with heptane glue and covered with water. Embryos at the end of stage 14 and 16 were selected for imaging dorsal closure and tracheal cells, respectively. Live imaging was performed at room temperature on an inverted TCS-sp5 confocal microscope (Leica) equipped with a 63× 1.4 NA plan Apo oil immersion objective and Hybrid detectors HyD, using Leica software. Stacks of 7–10 z sections (0.5 or 0.7 µm Z step size) were taken every 15 s for 10 min. Using ImageJ, a maximum intensity z-projection was then applied to use the plugin Filopodyan for filopodia reconstruction.

Human iPSC lines, culture, and imaging

For cortical differentiation, all cells were maintained at 5% CO_2 at 37°C in a humidified incubator. NDC1.2 (Israel et al., 2012) iPSCs were grown in Essential-8 medium (ThermoFisher) as feeder free cultures on Geltrex-coated (ThermoFisher) plates. Neuronal induction was

performed as described previously (Shi et al., 2012). In brief, iPSCs were passaged with 0.5 mM EDTA and plated at high density to reach 100% confluency in 24 h when neuronal induction was started (day 0). Essential-8 medium was changed to neuronal induction medium consisting of neuronal maintenance medium supplemented with 10 µm SB43152 (Tocris) and 1 µm Dorsomorphin (Tocris). The medium was changed daily until reaching day 12. On day 12, the neuroepithelial sheet was lifted off with Dispase (ThermoFisher), broken up to smaller clumps, and plated on laminin-coated (Sigma) plates in neuronal induction medium. On day 13, the medium was changed to neuronal maintenance medium supplemented with 20 ng/ml FGF2 (PeproTech). Medium was changed every other day, and FGF2 was withdrawn from the medium on day 17. Cells were split with Dispase at a 1:2 ratio when neuronal rosettes started to meet. On day 25, cells were disassociated with Accutase (ThermoFisher) and replated on laminin-coated plates. Until day 34, cells were expanded at a 1:2 ratio when they reached 90% confluency. On day 36, neurons were plated on laminin coated plates at 85,000 cells/cm^2 and used for subsequent experiments. Neuronal maintenance medium (1L) consists of 500 ml DMEM/F12 + Glutamax (ThermoFisher), 0.25 ml insulin (10 mg/ml; Sigma), 1 ml 2-mercaptoethanol (50 mM; ThermoFisher), 5 ml nonessential amino acids (100×; ThermoFisher), 5 ml sodium pyruvate (100 mM; Sigma), 2.5 ml penicillin/streptomycin (10,000 U/µl; ThermoFisher), 5 ml N2 (ThermoFisher), 10 ml B27 (ThermoFisher), 5 ml Glutamax (100×; ThermoFisher), and 500 ml Neurobasal (ThermoFisher) medium. Two-photon imaging of human neuronal filopodia: Human cortical neurons were transfected on day 38 with a plasmid expressing NeonGreen fluorescence protein from the human synapsin 1 promoter using Lipofectamin3000 (ThermoFisher) following the manufacturer's protocol. Neurons were kept in neuronal maintenance medium until they reached day 88. To reduce background fluorescence during two-photon imaging, the medium was changed to neuronal maintenance medium without phenol red DMEM/F12 + L-glutamin/phenol red (ThermoFisher). The inverted two-photon microscope (VIVO multiphoton; 3i) was equipped with a humidified incubator, and we performed imaging at 5% CO_2 at 37°C. NeonGreen was excited at 950 nm using a tunable pulsed laser (InSight DS+; Spectra Physics), and time-lapse image stacks of filopodia were taken over 30 min at 2-min time intervals using a 63× objective (X/Y pixel size, 0.053 µm; Z step size, 0.38 µm). Image stacks were exported to tiffs using Slidebook (3i) software.

Segmentation and tracking in ImageJ/Fiji

The full code of our plugin is publicly available at https://github.com/gurdon-institute/Filopodyan. Images are first processed with a LoG filter to reduce noise and enhance contrast of the features of interest.

$$\mathrm{LoG}: f(x,y) = \frac{-1}{\pi \times \sigma^4} \times \left(1 - \frac{x^2+y^2}{2\times\sigma^2}\right) \times e^{-\frac{x^2+y^2}{2\times\sigma^2}}.$$

The resulting images are binarized using a choice of autothresholding algorithms, and the largest object in the field of view is assumed to be the growth cone/cell body. The binary mask at each time point is segmented into the growth cone/cell body and filopodia by applying n erode operations, where n is the number required to remove all filopodia from the mask, followed by n dilate operations to restore the size of the resulting growth cone body mask. This final mask is subtracted from the original mask to leave only separate filopodia for analysis. For each of the segmented filopodia, ROIs are calculated at the base and tip defined by intersection with the growth cone body and the point furthest from it, respectively. Filopodia are tracked over time using a rapid one-step Hungarian linear assignment algorithm, with linking costs calculated using the following equation:

$$cost = \frac{dist(base_1, base_2) + dist(tip_1, tip_2)}{\sqrt{overlap\ area}} \delta T.$$

Tracks can be filtered using several different threshold values, and tracking errors in the resulting reconstruction can be manually corrected using a simple interface to delete filopodia from tracks and draw the desired links.

Measurement of metrics describing filopodial shape, dynamics and fluorescence

Length. An estimate of length is defined in Filopodyan coarsely as one half of perimeter of the protrusion ROI. Because this leads to an overestimation of length for short filopodia, we adjusted our perimeter length computation with a correction that substantially reduces the error in length estimation for short filopodia. This correction accounts for the contribution of base width and tip roundedness to perimeter length and subtracts an estimate of these quantities multiplied with a scaling factor. Thus, estimated length is defined as

$$\frac{Perimeter}{2} - \frac{(\pi-2)}{2}\sqrt{2\ln 2}\ \sigma px\ \min\left[\left(\frac{D}{w}\right)^2,\ 1\right].$$

This is derived from protrusion ends correction (tip correction, 1/4 circumference with radius $w/2$; base correction, $w/2$); width w is estimated for this purpose by the formula for full width at half maximum using user-defined σ of LoG (provided during segmentation step) and pixel width px ($w = 2\sqrt{2\ln 2}\ \sigma px$). Scaling factor $\min[(D/w)^2, 1]$ adjusts the degree of correction for protrusions whose width is greater than their Euclidean (base, tip) distance (D).

Straightness. Straightness is defined as

$$Straightness = Distance(tip, base)/Length$$
$$Waviness = 1 - Straightness.$$

Straightness is underestimated for short filopodia (and equally, waviness is overestimated for short filopodia), which in practice is not reliable for short structures. The plugin is not intended to look at branched structures. If applied to branched structures, straightness and waviness will be inaccurate as a measure of actual projection straightness and will instead reflect the degree of branching.

dL, the change in length between successive time points, is defined as $dL\ (T_n) = Length(T_n) - Length(T_{n-1})$. *dL* is affected by tip movement as well as base movement, which are more informative metrics; hence, *dL* was largely ignored in our analysis. *dL* could be useful when a measure of length change independent of corrections for position or direction is required.

Tip movement. Tip movement, or the rate of directional tip extension or retraction, provides a direct measure of the rate of tip extension or retraction between successive time points. Itis defined as direction-corrected tip movement (DCTM), calculated as the magnitude of the tip displacement vector from the preceding time point projected onto the vector connecting the base and the tip at a current time point:

$$DCTM = \|[Tip_{t-1},\ Tip_t]\| \quad : \quad [Base_t, Tip_t].$$

DCTM is closely related to tip speed and equals tip speed when the angle of filopodium is constant between successive time points. When the angle of a filopodium changes between successive time points (e.g., because of sideways movement of the tip), DCTM is corrected for that change in angle (e.g., so as not to overestimate extension if increased speed was caused by swinging of the filopodium). DCTM equals *dL* when the base is static and filopodium angle is constant. DCTM can be conceptualized as tip speed within a simplified one-dimensional

representation of the filopodium. We believe this approach is the best available readout for the rate of productive polymerization of actin filaments at filopodia tips during extension, or their breakdown during retraction, assuming no retrograde flow.

Filopodyan outputs a wide range of metrics representing the behavior of filopodia, and we anticipate that each user will wish to select those of interest for their own experiments and apply their own choice of statistical analysis. We applied downstream analysis to the output tables using scripts in R for our pipeline, but any program could be used, depending on the required functions. These scripts apply a tip movement filter to reject measurements outside the 0.5 the 99.5 percentile range (often caused by out of focus effects and reconstruction errors), smoothed with a five-step rolling mean. Tip movement is further divided into *tip extension rate* = DCTM, where DCTM > 32.5 nm/s, and *tip retraction rate* = DCTM, where DCTM < −32.5 nm/s.*Initial tip movement* = median DCTM over first 10 time points (0–20 s).

Base Movement. Base movement is the rate of directional base invasion or retraction, defined as

$$DCBM = \left\| [Base_{t-1}, Base_t] \right\| \quad : \quad [Base_t, Tip_t].$$

Direction-corrected base movement (DCBM) is directly analogous to DCTM as described in the Tip movement subsection. DCBM is further divided into *base invasion rate* = DCBM, where DCBM > 32.5 nm/s, and *base retraction rate* = DCBM, where DCBM < 32.5 nm/s. *Initial base movement* = median DCBM over first 10 time points (0–20 s).

Tip persistence. Tip persistence is a measure of consistency of tip movement across time. For each filopodium, the autocorrelation function is computed for the time series of its tip movement. Tip persistence is the root of this function (i.e., the time required for autocorrelation of tip movement for a filopodium to drop to zero). Tip movement was smoothed with a rolling mean filter (step size = 5) before the calculation to reduce noise.

Time extending/retracting/stalling. Time extending/retracting/stalling is the proportion of time the tip spent in any of the three states of movement. Extension time is consistent extension by more than 32.5 nm/s for 10 s, retraction time is consistent retraction by more than −32.5 nm/s for 10 s, and stalling time is tip movement between −32.5 and 32.5 nm for 10 s. Tip movement was smoothed with a rolling mean filter (step size = 5) before the calculation to reduce the effects caused by measurement noise.

Projection mean. Proj mean is the mean fluorescence intensity within the area reconstructed as protrusion (projection; cyan in Filopodyan overlay) in the channel set as measurement channel.

Base mean. This is the mean fluorescence intensity within the base area of the protrusion (orange in Filopodyan overlay) in the channel set as measurement channel.

Predicted base area/predicted base position is defined as the position on current boundary with minimum distance from the base at the preceding time point.

Tip mean. This is the mean fluorescence intensity within the area reconstructed as tip of protrusion (green in Filopodyan overlay) in the channel set as the measurement channel. Tip is defined as the point at the boundary with maximum distance from the base. The tip may be incorrectly assigned in backward turning, looping, or buckling filopodia.

Tip thresholded mean. This is the mean fluorescence intensity within Otsu-thresholded tip ROI in the channel set as measurement channel. This measure is useful when a significant proportion of the tip area has the same fluorescence intensity as signal background, separating tip signal from background.

Body mean. This is mean fluorescence intensity within the body area of the cell or growth cone (magenta in Filopodyan overlay) in the channel set as measurement channel.

Additional optional functionalities in Filopodyan

Tip fitting. Tip fitting to the measurement channel is done in a radius of $r = \sqrt{(processArea/2)/\pi}$, where 3 < r < 20 pixels. The tip position is set to the intensity weighted mean of the local intensity maxima coordinates and the new tip radius is set to $\sqrt{MSE}/2$, where MSE is the mean squared error of the maxima coordinates.

Fragment joining. Fragment joining is a useful option when parts of filopodia contain a weaker signal or are partially out of focus. Fragment joining ensures all disconnected fragments are connected to the growth cone by finding the shortest line connecting any two points on the boundaries and adding it to the binary mask. It connects fragments that are close together, then connects the joined fragments to the growth cone until they converge to a single structure over a maximum of 10 iterations.

Boundary visualization. Signal intensity along the boundary of the growth cone is measured for each point by taking the mean value of a small internal area in the specified channel, and the local velocity is estimated based on the change in intensity at the boundary coordinates over time in the unprocessed image (inspired by Barry et al., 2015). The boundary signal intensity and velocity values can be used to generate color-coded boundary images, kymographs showing change over time in 2D and cross-correlation plots showing the relationship between signal intensity and boundary extension or retraction.

Adaptive thresholding. The adaptive local thresholding function convolves the image with directional LoG kernels for the eight principal directions, thresholds the resulting images separately using the selected method, and combines them into a single mask with noise removed using a median filter.

Quantification of morphodynamic properties of filopodia in *Xenopus* RGCs growth cones

For phenotypic characterization of filopodial properties, time series of *Xenopus* growth cones expressing GAP-RFP, coexpressed with mNeonGreen, mNeonGreen-ENA, or mNeonGreen-VASP, were quantified with Filopodyan using GAP-RFP as the mapping channel with the following segmentation and filtering parameters: thresholding method: Renyi entropy, σ_{LoG} = 2.6, ED step = 4; tip fitting: disabled; filtering: min frames = 3, min max length = 1.8 µm, min length change = 0.1 µm, max mean waviness = 0.35. Except in the case of batch processing (Figs. 2 and S1), manual editing was applied to remove reconstructions if they were false positives, out of focus, looping, branching, crossing, or emanating from axon shaft, and obvious tracking errors were rectified. Correlation matrix visualizations (Fig. 3) were constructed with the R package corrplot (Wei and Simko, 2016). Visual representations of morphodynamic phenotype are constructed from data normalized such that the median of the control dataset equals 0, and one interquartile range of the control dataset equals 1. New filopodia were identified by downstream R scripts as the filopodia with min T > 1 and starting length < 2 µm to remove longer new reconstructions representing filopodia suddenly coming into focus. Initial speed of tip movement was defined as the median DCTM of the first 10 time points (20 s) in existence. Initial preformation fluorescence was defined as the mean of the last three time points before emergence. Full code is available at https://github.com/gurdon-institute/Filopodyan/tree/master/FilopodyanR (scripts Correlations.R and Correlations_DataInput.R and FilopodyanR modules 1, 2, and 3).

Quantification of base fluorescence before filopodium initiation

Time series of mNeonGreen-ENA– and mNeonGreen-VASP–expressing growth cones were reconstructed with Filopodyan v20170201 using GAP-RFP as the mapping channel and the following segmentation and filtering parameters: thresholding: Renyi entropy, $\sigma_{LoG} = 2.6$, ED = 4, number of base back frames = 20 (other segmentation options disabled); filtering: min start frame = 2, min frames = 3, min max length = 1.8 µm, min length change = 0.1 µm, max mean waviness = 0.38. Additional manual editing was applied as required to remove incorrect or unsuitable annotations (false positives, tracking errors, or filopodia arising from the axon shaft). Background measurements were subtracted from mean base fluorescence before normalizing to background-corrected mean body fluorescence. Full code is available at https://github.com/gurdon-institute/Filopodyan/tree/master/FilopodyanR (scripts Module 1.R, Module 1–2_BgCorrection.R, and BaseF.R).

Quantification of tip fluorescence

Time series of growth cones were reconstructed with Filopodyan using GAP-RFP as the mapping channel with the following parameters: thresholding: Huang, $\sigma_{LoG} = 4.01$, ED = 4; tip fitting: enabled, fragment joining: disabled; filtering: min frames = 3, min max length = 1.8 µm, max mean waviness = 0.38. Extensive manual editing was applied to ensure all reconstructed structures in all time points represented meaningful measurements, removing reconstructed tracks that were false positives, out of focus, branching, looping, or emanating from the axon shaft or whose tip ROIs were incorrectly positioned relative to tip signal. Background-subtracted thresholded tip fluorescence was normalized to background-subtracted body fluorescence in the corresponding time point. Full code is available at https://github.com/gurdon-institute/Filopodyan/tree/master/FilopodyanR (scripts Module 1.R and Module 1–2 BgCorrection.R).

Cross-correlation analysis and hierarchical clustering

For each filopodium, the value of the CCF between tip fluorescence (background corrected by the subtraction of background signal near the growth cone boundary and normalized to body fluorescence with equivalent background subtraction) and its DCTM (passed through 0.5 to 99.5 percentile filter and smoothed with five-step rolling mean) was calculated in R using the R Stats function ccf(). Filopodia with fewer than 17 time point measurements were excluded from analysis, because they were too short to generate meaningful randomizations. CCFs of all filopodia were fed into a hierarchical clustering analysis using Euclidean distance between CCFs at offsets between −6 and +6 s as a similarity measure. Heatmap visualizations were generated using heatmap.2() function from R package gplots (Warnes et al., 2016). For randomization controls, smoothed DCTM measurements for each filopodium were randomly reshuffled in blocks of eight time points to preserve their autocorrelation (similar to the value of their tip persistence), and the CCF values were recalculated for each randomized time series using the same method. CCFs from the randomized time series were then analyzed by hierarchical clustering in a manner identical to the original non-randomized dataset. To minimize bias arising from differences in cluster size, the resulting clusters were only accepted into the analysis if the number of filopodia in the top correlating subcluster was similar as in the original nonrandomized dataset to within 15% (arbitrary cutoff). CCFs for all the randomized filopodia in the top correlating subclusters of each randomization were recorded. Block randomization, clustering, and top correlating subcluster assessment were repeated until reaching 1,000 accepted randomization datasets. Full code is available at https://github.com/gurdon-institute/Filopodyan/tree/master/FilopodyanR (in FilopodyanR scripts CCF.R, CCF_Randomisations.R, and CCF_subcluster-analysis.R).

Discrete time Markov chain simulations

For each filopodium, its tip fluorescence (normalized background-corrected measurements) and tip movement (five-step rolling mean smoothed tip movement [DCTM]) were binned into nine equal-sized intervals to assign Markov states. The R package markovchain (Spedicato, 2016) was used to calculate transition probabilities between these states for each filopodium and to run 10,000 simulations (realizations) per filopodium transition matrix. The initial state of each filopodium was used as the starting state for all its corresponding simulations. A small fraction of filopodia produced invalid transition matrices (3 out of 45 in the ENA dataset and 4 out 76 in the VASP dataset), and these were discarded from the Markov chain analysis. Full code is available at https://github.com/gurdon-institute/Filopodyan/tree/master/FilopodyanR (FilopodyanR MarkovChains.R).

Online supplemental material

Fig. S1 shows a comparison of filopodia properties measured with and without manual editing of reconstruction. Fig. S2 shows tip and base movements in filopodia arising from protrusive or retractive events. Fig. S3 shows randomization control for the hierarchical clustering of cross-correlations between tip fluorescence and movement. Fig. S4 shows a Monte Carlo Markov chain method confirming the low likelihood of observed correlations between ENA and VASP tip fluorescence and tip movement occurring by chance. Fig. S5 shows an assessment of robustness in cross-correlation against subcluster size. Video 1 is a time-lapse video of a *Xenopus* RGC growth cone, imaged with HILO illumination on a TIRF imaging system and segmented with Filopodyan. Video 2 shows *Drosophila* tracheal cells imaged by line-scanning confocal microscopy and segmented with Filopodyan. Video 3 shows *Drosophila* leading edge cells during dorsal closure imaged by line-scanning confocal microscopy and segmented with Filopodyan. Video 4 shows dendritic filopodia in iPSC-derived human cortical neurons, imaged by two-photon microscopy and segmented with Filopodyan. Video 5. shows mNeonGreen-ENA localization during formation of new filopodia in an RGC growth cone. Video 6 shows localization of mNeonGreen-VASP before filopodia formation in an RGC growth cone. Video 7 shows localization of mNeonGreen-VASP in an RGC growth cone during formation of a single filopodium in an RGC growth cone. Video 8 shows mNeonGreen-ENA localization in filopodia tips during extension in an RGC growth cone imaged with HILO illumination. Video 9 shows mNeonGreen-ENA localization in filopodia tips during extension in an RGC growth cone. Video 10 shows two filopodia tips showing differential response to mNeonGreen-VASP accumulation in an RGC growth cone. Table S1 lists the full phenotypic measurements and associated statistics. The complete data tables outputted by Filopodyan of growth cone filopodia parameters and fluorescence intensities that were used as the source of further analysis are provided as a zipped data file.

Acknowledgments

The authors would like to thank the Gallop and Harris/Holt laboratories for insightful suggestions; Ulrich Dobramysl, David Jordan, and Edouard Hanezzo for discussions on data analysis; and Edouard Hanezzo and Ulrich Dobramysl for critical reading of the manuscript.

J.L. Gallop and V. Urbančič are supported by the Wellcome Trust (WT095829AIA). J. Mason and B. Richier are supported by the European Research Council (281971). C.E. Holt is supported by the Wellcome Trust (program grant 085314) and the European Research Council (advanced grant 322817). The Gurdon Institute is funded by the Wellcome Trust (203144) and Cancer Research UK (C6946/A24843).

The authors declare no competing financial interests.

Author contributions: V. Urbančič, C.E. Holt, and J.L. Gallop conceived the study and designed the experiments. J. Mason created the DNA constructs. V. Urbančič conducted the experiments shown in Figs. 2 A, 3, 4, 5, and 6 together with B. Richier (Fig. 2, B and C) and M. Peter and F.J. Livesey (Fig. 2 D). R. Butler developed the Fiji plugin in Java. V. Urbančič developed scripts in R and data analysis. V. Urbančič and J.L. Gallop wrote the manuscript with contributions from all authors.

Submitted: 22 May 2017
Revised: 28 June 2017
Accepted: 6 July 2017

References

Applewhite, D.A., M. Barzik, S. Kojima, T.M. Svitkina, F.B. Gertler, and G.G. Borisy. 2007. Ena/VASP proteins have an anti-capping independent function in filopodia formation. *Mol. Biol. Cell.* 18:2579–2591. http://dx.doi.org/10.1091/mbc.E06-11-0990

Atkinson-Leadbeater, K., C.L. Hehr, J. Johnston, G. Bertolesi, and S. McFarlane. 2016. EGCG stabilizes growth cone filopodia and impairs retinal ganglion cell axon guidance. *Dev. Dyn.* 245:667–677. http://dx.doi.org/10.1002/dvdy.24406

Barry, D.J., C.H. Durkin, J.V. Abella, and M. Way. 2015. Open source software for quantification of cell migration, protrusions, and fluorescence intensities. *J. Cell Biol.* 209:163–180. http://dx.doi.org/10.1083/jcb.201501081

Barzik, M., L.M. McClain, S.L. Gupton, and F.B. Gertler. 2014. Ena/VASP regulates mDia2-initiated filopodial length, dynamics, and function. *Mol. Biol. Cell.* 25:2604–2619. http://dx.doi.org/10.1091/mbc.E14-02-0712

Bentley, D., and A. Toroian-Raymond. 1986. Disoriented pathfinding by pioneer neurone growth cones deprived of filopodia by cytochalasin treatment. *Nature.* 323:712–715. http://dx.doi.org/10.1038/323712a0

Bilancia, C.G., J.D. Winkelman, D. Tsygankov, S.H. Nowotarski, J.A. Sees, K. Comber, I. Evans, V. Lakhani, W. Wood, T.C. Elston, et al. 2014. Enabled negatively regulates diaphanous-driven actin dynamics in vitro and in vivo. *Dev. Cell.* 28:394–408. http://dx.doi.org/10.1016/j.devcel.2014.01.015

Bisi, S., A. Disanza, C. Malinverno, E. Frittoli, A. Palamidessi, and G. Scita. 2013. Membrane and actin dynamics interplay at lamellipodia leading edge. *Curr. Opin. Cell Biol.* 25:565–573. http://dx.doi.org/10.1016/j.ceb.2013.04.001

Brown, M.E., and P.C. Bridgman. 2003. Retrograde flow rate is increased in growth cones from myosin IIB knockout mice. *J. Cell Sci.* 116:1087–1094. http://dx.doi.org/10.1242/jcs.00335

Charras, G.T., C.K. Hu, M. Coughlin, and T.J. Mitchison. 2006. Reassembly of contractile actin cortex in cell blebs. *J. Cell Biol.* 175:477–490. http://dx.doi.org/10.1083/jcb.200602085

Chen, T.J., S. Gehler, A.E. Shaw, J.R. Bamburg, and P.C. Letourneau. 2006. Cdc42 participates in the regulation of ADF/cofilin and retinal growth cone filopodia by brain derived neurotrophic factor. *J. Neurobiol.* 66:103–114. http://dx.doi.org/10.1002/neu.20204

Chien, C.B., D.E. Rosenthal, W.A. Harris, and C.E. Holt. 1993. Navigational errors made by growth cones without filopodia in the embryonic *Xenopus* brain. *Neuron.* 11:237–251. http://dx.doi.org/10.1016/0896-6273(93)90181-P

Disanza, A., S. Bisi, M. Winterhoff, F. Milanesi, D.S. Ushakov, D. Kast, P. Marighetti, G. Romet-Lemonne, H.M. Müller, W. Nickel, et al. 2013. CDC42 switches IRSp53 from inhibition of actin growth to elongation by clustering of VASP. *EMBO J.* 32:2735–2750. http://dx.doi.org/10.1038/emboj.2013.208

Dwivedy, A., F.B. Gertler, J. Miller, C.E. Holt, and C. Lebrand. 2007. Ena/VASP function in retinal axons is required for terminal arborization but not pathway navigation. *Development.* 134:2137–2146. http://dx.doi.org/10.1242/dev.002345

Faix, J., and K. Rottner. 2006. The making of filopodia. *Curr. Opin. Cell Biol.* 18:18–25. http://dx.doi.org/10.1016/j.ceb.2005.11.002

Falk, J., J. Drinjakovic, K.M. Leung, A. Dwivedy, A.G. Regan, M. Piper, and C.E. Holt. 2007. Electroporation of cDNA/Morpholinos to targeted areas of embryonic CNS in *Xenopus*. *BMC Dev. Biol.* 7:107. http://dx.doi.org/10.1186/1471-213X-7-107

Gehler, S., G. Gallo, E. Veien, and P.C. Letourneau. 2004. p75 neurotrophin receptor signaling regulates growth cone filopodial dynamics through modulating RhoA activity. *J. Neurosci.* 24:4363–4372. http://dx.doi.org/10.1523/JNEUROSCI.0404-04.2004

Geraldo, S., U.K. Khanzada, M. Parsons, J.K. Chilton, and P.R. Gordon-Weeks. 2008. Targeting of the F-actin-binding protein drebrin by the microtubule plus-tip protein EB3 is required for neuritogenesis. *Nat. Cell Biol.* 10:1181–1189. http://dx.doi.org/10.1038/ncb1778

Hendricusdottir, R., and J.H. Bergmann. 2014. F-dynamics: Automated quantification of dendrite filopodia dynamics in living neurons. *J. Neurosci. Methods.* 236:148–156. http://dx.doi.org/10.1016/j.jneumeth.2014.08.016

Hotulainen, P., and C.C. Hoogenraad. 2010. Actin in dendritic spines: Connecting dynamics to function. *J. Cell Biol.* 189:619–629. http://dx.doi.org/10.1083/jcb.201003008

Israel, M.A., S.H. Yuan, C. Bardy, S.M. Reyna, Y. Mu, C. Herrera, M.P. Hefferan, S. Van Gorp, K.L. Nazor, F.S. Boscolo, et al. 2012. Probing sporadic and familial Alzheimer's disease using induced pluripotent stem cells. *Nature.* 482:216–220.

Jacquemet, G., H. Hamidi, and J. Ivaska. 2015. Filopodia in cell adhesion, 3D migration and cancer cell invasion. *Curr. Opin. Cell Biol.* 36:23–31. http://dx.doi.org/10.1016/j.ceb.2015.06.007

Jacquemet, G., I. Paatero, A. Carisey, A. Padzik, J. Orange, H. Hamidi, and J. Ivaska. 2017. FiloQuant reveals increased filopodia density during DCIS progression. *bioRxiv.* doi:http://dx.doi.org/10.1101/125047 (Preprint posted April 7, 2017)

Kalil, K., and E.W. Dent. 2014. Branch management: Mechanisms of axon branching in the developing vertebrate CNS. *Nat. Rev. Neurosci.* 15:7–18. http://dx.doi.org/10.1038/nrn3650

Krause, M., and A. Gautreau. 2014. Steering cell migration: Lamellipodium dynamics and the regulation of directional persistence. *Nat. Rev. Mol. Cell Biol.* 15:577–590. http://dx.doi.org/10.1038/nrm3861

Lanier, L.M., M.A. Gates, W. Witke, A.S. Menzies, A.M. Wehman, J.D. Macklis, D. Kwiatkowski, P. Soriano, and F.B. Gertler. 1999. Mena is required for neurulation and commissure formation. *Neuron.* 22:313–325. http://dx.doi.org/10.1016/S0896-6273(00)81092-2

Lebrand, C., E.W. Dent, G.A. Strasser, L.M. Lanier, M. Krause, T.M. Svitkina, G.G. Borisy, and F.B. Gertler. 2004. Critical role of Ena/VASP proteins for filopodia formation in neurons and in function downstream of netrin-1. *Neuron.* 42:37–49. http://dx.doi.org/10.1016/S0896-6273(04)00108-4

Lee, K., J.L. Gallop, K. Rambani, and M.W. Kirschner. 2010. Self-assembly of filopodia-like structures on supported lipid bilayers. *Science.* 329:1341–1345. http://dx.doi.org/10.1126/science.1191710

Lee, K., H.L. Elliott, Y. Oak, C.T. Zee, A. Groisman, J.D. Tytell, and G. Danuser. 2015. Functional hierarchy of redundant actin assembly factors revealed by fine-grained registration of intrinsic image fluctuations. *Cell Syst.* 1:37–50. http://dx.doi.org/10.1016/j.cels.2015.07.001

Leung, K.M., and C.E. Holt. 2008. Live visualization of protein synthesis in axonal growth cones by microinjection of photoconvertible Kaede into *Xenopus* embryos. *Nat. Protoc.* 3:1318–1327. http://dx.doi.org/10.1038/nprot.2008.113

Lin, A.C., C.L. Tan, C.L. Lin, L. Strochlic, Y.S. Huang, J.D. Richter, and C.E. Holt. 2009. Cytoplasmic polyadenylation and cytoplasmic polyadenylation element-dependent mRNA regulation are involved in *Xenopus* retinal axon development. *Neural Dev.* 4:8. http://dx.doi.org/10.1186/1749-8104-4-8

Lohmann, C., and T. Bonhoeffer. 2008. A role for local calcium signaling in rapid synaptic partner selection by dendritic filopodia. *Neuron.* 59:253–260. http://dx.doi.org/10.1016/j.neuron.2008.05.025

Machacek, M., L. Hodgson, C. Welch, H. Elliott, O. Pertz, P. Nalbant, A. Abell, G.L. Johnson, K.M. Hahn, and G. Danuser. 2009. Coordination of Rho GTPase activities during cell protrusion. *Nature.* 461:99–103. http://dx.doi.org/10.1038/nature08242

Mallavarapu, A., and T. Mitchison. 1999. Regulated actin cytoskeleton assembly at filopodium tips controls their extension and retraction. *J. Cell Biol.* 146:1097–1106. http://dx.doi.org/10.1083/jcb.146.5.1097

Martin, K., A. Reimann, R.D. Fritz, H. Ryu, N.L. Jeon, and O. Pertz. 2016. Spatio-temporal co-ordination of RhoA, Rac1 and Cdc42 activation during prototypical edge protrusion and retraction dynamics. *Sci. Rep.* 6:21901. http://dx.doi.org/10.1038/srep21901

Mattila, P.K., and P. Lappalainen. 2008. Filopodia: Molecular architecture and cellular functions. *Nat. Rev. Mol. Cell Biol.* 9:446–454. http://dx.doi.org/10.1038/nrm2406

McConnell, R.E., J. Edward van Veen, M. Vidaki, A.V. Kwiatkowski, A.S. Meyer, and F.B. Gertler. 2016. A requirement for filopodia extension toward Slit during Robo-mediated axon repulsion. *J. Cell Biol.* 213:261–274. http://dx.doi.org/10.1083/jcb.201509062

Nieuwkoop, P., and J. Faber. 1967. The Normal Table of *Xenopus laevis* (Daudin). North-Holland Publishing Company, Amsterdam. 282 pp.

Nilufar, S., A.A. Morrow, J.M. Lee, and T.J. Perkins. 2013. FiloDetect: Automatic detection of filopodia from fluorescence microscopy images. *BMC Syst. Biol.* 7:66. http://dx.doi.org/10.1186/1752-0509-7-66

Nowotarski, S.H., N. McKeon, R.J. Moser, and M. Peifer. 2014. The actin regulators Enabled and Diaphanous direct distinct protrusive behaviors in different tissues during *Drosophila* development. *Mol. Biol. Cell.* 25:3147–3165. http://dx.doi.org/10.1091/mbc.E14-05-0951

O'Connor, T.P., J.S. Duerr, and D. Bentley. 1990. Pioneer growth cone steering decisions mediated by single filopodial contacts in situ. *J. Neurosci.* 10:3935–3946.

R Core Team. 2016. R: A language and environment for statistical computing. R Foundation for Statistical Computing, Vienna, Austria.

Rottner, K., B. Behrendt, J.V. Small, and J. Wehland. 1999. VASP dynamics during lamellipodia protrusion. *Nat. Cell Biol.* 1:321–322. http://dx.doi.org/10.1038/13040

Saarikangas, J., N. Kourdougli, Y. Senju, G. Chazal, M. Segerstråle, R. Minkeviciene, J. Kuurne, P.K. Mattila, L. Garrett, S.M. Hölter, et al. 2015. MIM-induced membrane bending promotes dendritic spine initiation. *Dev. Cell.* 33:644–659. http://dx.doi.org/10.1016/j.devcel.2015.04.014

Saha, T., I. Rathmann, A. Viplav, S. Panzade, I. Begemann, C. Rasch, J. Klingauf, M. Matis, and M. Galic. 2016. Automated analysis of filopodial length and spatially resolved protein concentration via adaptive shape tracking. *Mol. Biol. Cell.* 27:3616–3626. http://dx.doi.org/10.1091/mbc.E16-06-0406

Sánchez-Soriano, N., C. Gonçalves-Pimentel, R. Beaven, U. Haessler, L. Ofner-Ziegenfuss, C. Ballestrem, and A. Prokop. 2010. *Drosophila* growth cones: A genetically tractable platform for the analysis of axonal growth dynamics. *Dev. Neurobiol.* 70:58–71.

Schindelin, J., I. Arganda-Carreras, E. Frise, V. Kaynig, M. Longair, T. Pietzsch, S. Preibisch, C. Rueden, S. Saalfeld, B. Schmid, et al. 2012. Fiji: An open-source platform for biological-image analysis. *Nat. Methods.* 9:676–682. http://dx.doi.org/10.1038/nmeth.2019

Shaner, N.C., G.G. Lambert, A. Chammas, Y. Ni, P.J. Cranfill, M.A. Baird, B.R. Sell, J.R. Allen, R.N. Day, M. Israelsson, et al. 2013. A bright monomeric green fluorescent protein derived from *Branchiostoma lanceolatum*. *Nat. Methods.* 10:407–409. http://dx.doi.org/10.1038/nmeth.2413

Shi, Y., P. Kirwan, and F.J. Livesey. 2012. Directed differentiation of human pluripotent stem cells to cerebral cortex neurons and neural networks. *Nat. Protoc.* 7:1836–1846. http://dx.doi.org/10.1038/nprot.2012.116

Spedicato, G.A. 2016. markovchain: Easy handling of discrete time Markov chains. Available at https://cran.r-project.org/package=markovchain (package version: 0.6.6).

Svitkina, T.M., E.A. Bulanova, O.Y. Chaga, D.M. Vignjevic, S. Kojima, J.M. Vasiliev, and G.G. Borisy. 2003. Mechanism of filopodia initiation by reorganization of a dendritic network. *J. Cell Biol.* 160:409–421. http://dx.doi.org/10.1083/jcb.200210174

Tárnok, K., M. Gulyás, N. Bencsik, K. Ferenc, K. Pfizenmaier, A. Hausser, and K. Schlett. 2015. A new tool for the quantitative analysis of dendritic filopodial motility. *Cytometry A.* 87:89–96. http://dx.doi.org/10.1002/cyto.a.22569

Tokunaga, M., N. Imamoto, and K. Sakata-Sogawa. 2008. Highly inclined thin illumination enables clear single-molecule imaging in cells. *Nat. Methods.* 5:159–161. http://dx.doi.org/10.1038/nmeth1171

Tsygankov, D., C.G. Bilancia, E.A. Vitriol, K.M. Hahn, M. Peifer, and T.C. Elston. 2014. CellGeo: A computational platform for the analysis of shape changes in cells with complex geometries. *J. Cell Biol.* 204:443–460. http://dx.doi.org/10.1083/jcb.201306067

Warnes, G.R., B. Bolker, L. Bonebakker, R. Gentleman, W.H.A. Liaw, T. Lumley, M. Maechler, A. Magnusson, S. Moeller, M. Schwartz, and B. Venables. 2016. gplots: Various R programming tools for plotting data. Available at https://cran.r-project.org/package=gplots (package version: 3.0.1).

Wei, T., and V. Simko. 2016. corrplot: Visualization of a correlation matrix. Available at https://cran.r-project.org/package=corrplot (package version: 0.77).

Xu, T., X. Yu, A.J. Perlik, W.F. Tobin, J.A. Zweig, K. Tennant, T. Jones, and Y. Zuo. 2009. Rapid formation and selective stabilization of synapses for enduring motor memories. *Nature.* 462:915–919. http://dx.doi.org/10.1038/nature08389

Yang, C., and T. Svitkina. 2011. Filopodia initiation: Focus on the Arp2/3 complex and formins. *Cell Adhes. Migr.* 5:402–408. http://dx.doi.org/10.4161/cam.5.5.16971

Yang, G., F. Pan, and W.B. Gan. 2009. Stably maintained dendritic spines are associated with lifelong memories. *Nature.* 462:920–924. http://dx.doi.org/10.1038/nature08577

Zheng, J.Q., J.J. Wan, and M.M. Poo. 1996. Essential role of filopodia in chemotropic turning of nerve growth cone induced by a glutamate gradient. *J. Neurosci.* 16:1140–1149.

Ziv, N.E., and S.J. Smith. 1996. Evidence for a role of dendritic filopodia in synaptogenesis and spine formation. *Neuron.* 17:91–102. http://dx.doi.org/10.1016/S0896-6273(00)80283-4